Stability-corrected wind profile model for complex mountainous terrain based on turbulence analysis

Tingyuan Yan[a], Jingxi Qin[c,*], Mingjin Zhang[a,b,d], Chengtao Zhang[a], Jinxiang Zhang[a], Yongle Li[a,b,d]

[a] *Department of Bridge Engineering, Southwest Jiaotong University, Chengdu, 610031, China*

[b] *State Key Laboratory of Bridge Intelligent and Green Construction, Southwest Jiaotong University, Chengdu 611756, Sichuan, China*

[c] *Department of Civil and Environmental Engineering, The Hong Kong Polytechnic University, Kowloon, Hong Kong, China*

[d] *Wind Engineering Key Laboratory of Sichuan Province, Southwest Jiaotong University, Chengdu 610031, China*

**Corresponding Author: Jingxi Qin, jingxi.qin@polyu.edu.hk*

Abstract: In complex mountainous terrain, the vertical wind field is characterized by pronounced nonstationarity, elevated mean wind speeds, and intricate turbulence structures, all of which exert considerable influence on boundary-layer environments and related applications. This study proposes an improved atmospheric stability-corrected wind profile model that integrates both mean flow and turbulence characteristics. The model constructs an empirical stability function within the Monin–Obukhov Similarity Theory (MOST) framework and explicitly incorporates the terrain-specific behavior of universal functions in mountainous environments. In this model, atmospheric stability is computed from a discrete wavelet transform (DWT)-based decomposition of wind velocity signals, which effectively captures nonstationary fluctuations in mountain wind fields. The optimal decomposition level is determined via cospectral analysis of the coupled transport between turbulent velocity and temperature, while the decomposition performance is further evaluated through correlation analysis and evolutionary power spectral density (EPSD). Finally, the proposed model is validated using long-term field measurements from a mountainous site and demonstrated through a case study, confirming its capability to accurately reconstruct stability-corrected wind profiles up to several hundred meters above ground.

Keywords: Field measurements; Wind profile; Mountainous terrain; Wind characteristics; Atmospheric stability; Turbulent characteristics

1 Introduction

With the continued expansion of human activities, wind environments have become increasingly complex, particularly in mountainous terrain [1-2]. This complexity is reflected not only in the diverse distribution of wind profiles [3] but also in the strongly nonstationary nature of turbulence structures [4], posing significant challenges for complex-terrain meteorology and climatology [5], wind energy assessment [6], pollutant dispersion prediction [7], and structural design [8-9]. In such regions, the installation of tall meteorological towers, commonly used in large urban environments, is often impractical due to economic and topographic constraints, particularly in deep valleys [10]. As a result, high-frequency wind measurements are usually limited to near-surface meteorological masts. At the same time, remote-sensing instruments widely applied in complex terrain, such as Lidar and SODAR [11-14], mainly provide low-frequency mean wind profiles and are insufficient to capture turbulence characteristics directly. Therefore, developing a wind speed profile model tailored to complex mountainous terrain, one that integrates mean flow and turbulence structure to reveal their vertical coupling, is essential for boundary-layer environments and related applications.

The Monin–Obukhov Similarity Theory (MOST) is a classical framework for wind profile corrections that jointly characterizes mean wind flow and turbulence transport by accounting for atmospheric stability, under the assumption that turbulent fluxes are independent of height [15-17]. According to MOST-based corrections, turbulence eddies and vertical heat transport are more active under unstable atmospheric conditions, which tends to suppress horizontal mean wind speed [18]. In contrast, under stable atmospheric conditions, turbulent exchange is weaker, and flow tends to stratify, often resulting in enhanced horizontal winds , typically accompanied by clear-air radiative cooling and nighttime low-level jets [18-19]. Based on the distinct turbulent features associated with different stability conditions, researchers have developed widely used empirical functions that enable mutual correction and derivation between wind profiles and turbulence structures , facilitating the accurate construction of vertical wind structure models [21-23]. Therefore, on typical synoptic-scale wind days, surface heating during the daytime induces upward heat flux, which enhances vertical turbulence transport , forming unstable atmospheric conditions [24]. After sunset, the direction of surface heat flux reverses, resulting in a stable stratified atmosphere where vertical

turbulence weakens or becomes confined within layers [25].

MOST-based corrections have been applied across diverse terrains and regions worldwide. Over flat surfaces, Kansas wheat-field observations set classical benchmarks [26]. Urban studies in Hamburg and Torino examined built-up effects [27-28], while marine measurements along China's southeastern coast demonstrated applicability under typhoon winds [29]. Highland investigations in southeastern Mexico and Colorado extended MOST to elevated, thermally heterogeneous sites [30-31]. Together, these studies highlight its adaptability across terrain types and broad climatic zones. However, certain thermally driven and topographically complex wind environments present unique challenges to conventional MOST-based approaches.

As human activity expands, convective phenomena driven by surface temperature differences, such as urban heat island winds in large metropolitan areas [32], sea–land breezes in coastal regions [33], and thermally-induced winds in complex mountainous terrain [34-35], have become increasingly prominent and often exhibit wind-temperature consistency. In these cases, both wind speed and temperature rise after sunrise and typically peak in the afternoon. Although unstable atmospheric conditions may still suppress local weather-driven wind, intense winds of primary concern to wind engineering applications may already be present at structural locations. Moreover, complex terrain differs substantially from flat terrain, with more intricate turbulence structures and a higher degree of nonstationarity [36-37]. Sudden intense wind events in mountainous areas significantly influence turbulence stability, resulting in pronounced spatiotemporal variability in wind fields [38-39]. Such phenomena have been observed across diverse geographical settings, including severe windstorms generated by high-amplitude gap flows in Colorado [40], mountain waves over the Pyrenees [41], and widespread gust events in the mountainous regions of southwestern China [42]. This complexity challenges the applicability of traditional correction models in mountainous environments, underscoring the necessity to extend MOST-based atmospheric stability-corrected wind profile models to better fit complex terrain. A prerequisite for constructing such models is the effective identification of turbulence characteristics specific to complex topography.

Turbulence characterization relies on the separation of high-frequency wind speed signals into trend components (representing mean flow) and detail components (representing fluctuating

wind) [42]. From the perspective of structural wind loading, this distinction corresponds to static and dynamic components [44-45], where the former is governed by mean wind speed, and the latter is calculated based on turbulent fluctuations. The modelling approaches and solution procedures differ considerably between the two components [46]. In terms of flux transport, horizontal transfers of heat and momentum are generally attributed to mean wind flow, while vertical transport is dominated by small-scale eddies across vertical interfaces [47]. As a result, nonstationarity within the fluctuating component can affect both structural responses and flux estimations, potentially leading to misinterpretation of the wind environment. However, traditional time-window-based separation methods are often inadequate under highly nonstationary wind conditions [48]. To address this issue, time-varying methods have been introduced to identify nonstationary components. Among them, the moving average (MA) method [48] is widely applied to extract time-varying mean wind speed. Time-frequency techniques such as discrete wavelet transform (DWT) [50] and empirical mode decomposition (EMD) [51] have also been extensively employed. Specifically, wavelet decomposition progressively concentrates on lower-frequency content across levels, yielding a low-frequency approximation subseries together with several high-frequency detail subseries. It performs well in extracting useful information and mitigating wind-speed fluctuations [52]. However, it can be limited in adaptivity, so careful selection of the mother wavelet and the number of decomposition levels is required. In recent years, empirical mode decomposition (EMD) and its improved variants have been widely applied in the domain of turbulence analysis [53-55]. EMD adaptively decomposes a time series, based on local characteristics, into intrinsic mode functions (IMFs) spanning different frequency bands and a residual, thereby improving decomposition performance. Several enhanced EMD methods [56] have proven highly effective for analyzing nonlinear and nonstationary processes. These methods can be interpreted as sets of band-pass filters, in which the high-frequency components represent stationary fluctuations. In complex mountainous terrain characterized by pronounced nonstationarity, time–frequency approaches have been widely applied and have yielded substantial progress, which include turbulence parameter studies on gust factor [57], turbulence intensity [58], and integral length scales [59]; the identification of special wind events associated with mixed wind systems [60]; the development of probability distribution model [61] and turbulence spectra model [62]. However, although time–

frequency decomposition is a key approach for extracting turbulent fluctuations in nonstationary wind fields, existing field studies provide limited insight into how it affects the coupling between fluxes and turbulent transport. This knowledge gap directly affects the determination of atmospheric stability in nonstationary wind fields and the derivation of stability-corrected wind profile models. Therefore, a comprehensive investigation that jointly evaluates the impacts of time-frequency algorithms and the relationship between turbulence and flux is needed, particularly in complex mountainous terrain.

To overcome the limited applicability of traditional stability-corrected wind profile models in complex mountainous terrain, and to address the unresolved coupling between fluxes and turbulent transport under time–frequency decomposition in nonstationary wind fields, this study carried out long-term field measurements in the mountainous region of southwestern China. Based on the measurement data, an atmospheric stability-corrected wind profile model tailored specifically to mountainous environments was developed, together with methods for extracting turbulent fluctuations and their associated fluxes. The remainder of this paper is structured as follows: Section 2 introduces the measurement site and data acquisition methods; Section 3 presents the turbulence decomposition approach and the resulting atmospheric stability analysis applicable to complex terrain; Section 4 derives the improved wind profile correction model and verifies its performance using observational data and a case study; and Section 5 summarizes the main conclusions. The research framework is shown in Fig. 1.

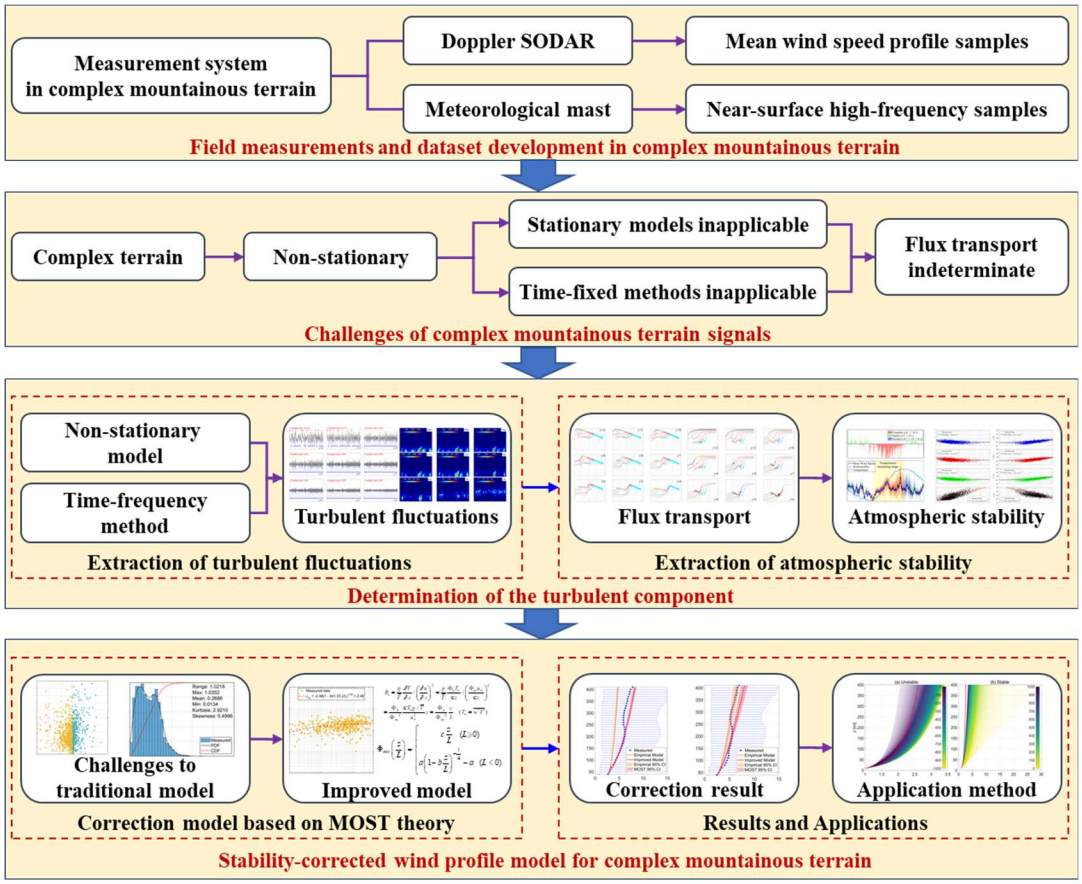

Fig. 1 Schematic diagram of the research framework

2 Measurement site and data acquisition methods

The measurement data used to derive the new wind profile correction model were obtained from long-term measurements conducted in the mountainous region of southwestern China. Fig. 2 shows the specific installation locations of the measurement system at the Jinan Bridge site and the topographic features of the surrounding study area.

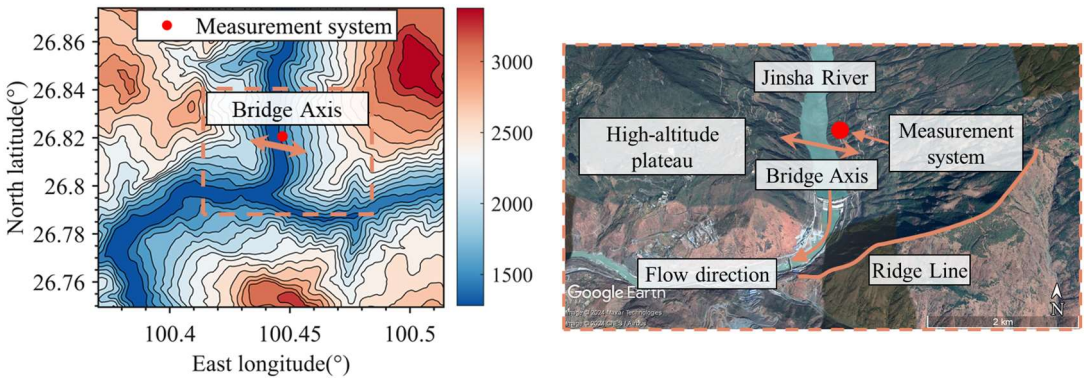

(a) Topographical map (b) Geomorphology map

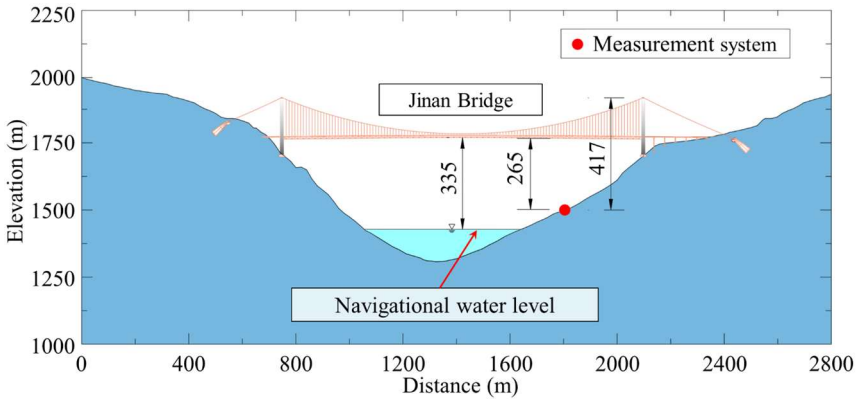

(c) Schematic of the Jinan Bridge

Fig. 2 Topography and geomorphology around the measurement site

The measurement system is situated on the eastern bank of the Jinsha River, which flows southward through a north–south oriented deep canyon. The surrounding terrain is characterized by steep mountains exceeding 3,000 m in elevation on the eastern, western, and southern sides. At the canyon entrance, a high plateau lies to the southwest and a steep ridge borders the southeast. The measurement system was installed at an elevation of 1,498 m, approximately 70 m above the navigational water level of the Jinsha River. It is located about 265 m below the main span of the Jinan Bridge, which crosses the deep canyon with a span length of 1,386 m.

The measurement system consists of a meteorological mast and a Doppler SODAR. The specific configurations of the two instruments are shown in Fig. 3.

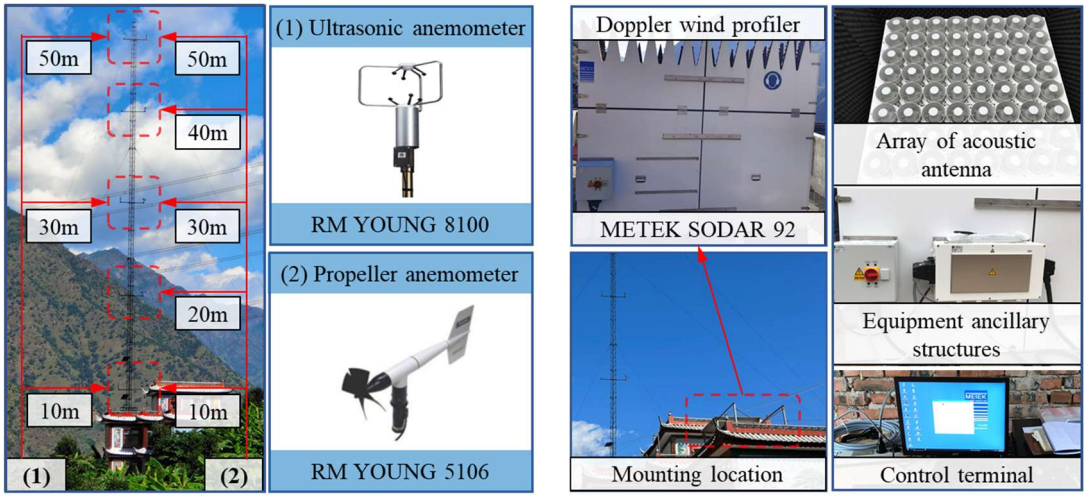

(a) Meteorological mast (b) SODAR system

Fig. 3 Composition of the field measurement system

As shown in Fig. 3a, three triaxial sonic anemometers (RM Young 8100) were mounted at 10 m, 30 m, and 50 m on the meteorological mast to measure three-dimensional wind velocity and air temperature at 10 Hz. Five biaxial propeller anemometers (RM Young 5106) were installed at

heights from 10 m to 50 m (in 10 m intervals) to record horizontal wind speed and wind direction at 1 Hz. The observation campaign spanned 45 months (January 2017 to September 2020). After removing outliers and interpolating missing values, 858 days of valid high-frequency wind and temperature data were retained. In this study, turbulence analysis near the surface is based on 50 m and 10 m sonic anemometers measurements.

As shown in Fig. 3b, the SODAR was installed at the base of the meteorological mast and configured to measure wind profiles from 40 m to 410 m above ground level at 10 m intervals, covering 38 vertical points. It recorded 10-minute mean three-dimensional wind velocity components at each level. After excluding transmission errors and invalid records, a total of 219 days of valid wind profile data were obtained between April 2017 and May 2018.

The three-dimensional wind velocity data obtained from the sonic anemometers and SODAR are used to calculate the fundamental wind parameters. The calculations of mean wind speed $\bar{U}$ (m/s), mean wind direction φ (°) and mean angle of attack α(°) used in the analysis are as follows:

$$\bar{U} = \sqrt{\bar{U}_x^2 + \bar{U}_y^2 + \bar{U}_z^2} \tag{1}$$

$$\varphi = \tan^{-1}\left(\frac{\bar{U}_x}{\bar{U}_y}\right) \quad \alpha = \tan^{-1}\left(\frac{\bar{U}_z}{\sqrt{\bar{U}_x^2 + \bar{U}_y^2}}\right) \tag{2}$$

where U_x represents the west-to-east component, U_y represents the south-to-north component, and U_z represents the downward-to-upward component. Wind direction indicates the horizontal inflow orientation, while the angle of attack represents the inclination of the wind vector relative to the horizontal plane.

Atmospheric stability is calculated as follows:

$$u_* = \left(\overline{u'w'}^2 + \overline{v'w'}^2\right)^{\frac{1}{4}} \tag{3}$$
$$H_* = \overline{w'T'}$$

$$L = -\frac{u_*^3}{\kappa \frac{g}{T} H_*} \tag{4}$$

where u, v, and w denote the fluctuating velocity components along the wind coordinate system, κ is the von Karman constant, g is the gravitational acceleration, and T is the air temperature. Both the numerator (friction velocity u_*) and the denominator (heat flux $\overline{w'T'}$) are calculated using the

eddy covariance method. Their ratio is used in the calculation of L, known as the Obukhov length, allowing the relative influence of thermal buoyancy and shear-driven turbulence at the site to be evaluated. The sign of L indicates the atmospheric stability:

(1) A positive L corresponds to a stable atmosphere.

(2) A negative L indicates an unstable atmosphere.

(3) If the absolute value is large, the atmosphere is considered to be close to neutral.

Fig. 4 presents two representative wind events in mountainous terrain and their corresponding wind profiles. Subplot (1) shows the atmospheric stability time series. Subplot (2) displays the high-frequency wind speed time series, color-coded by the stability classes in (1); timestamps used for the wind profiles are marked. Subplot (3) presents the typical wind profiles.

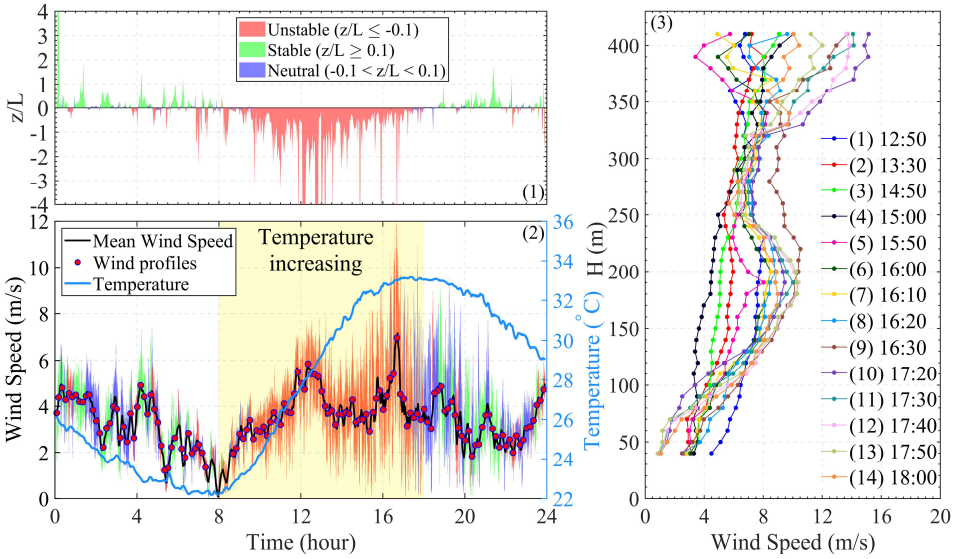

(a) Event1 (June 7, 2017)

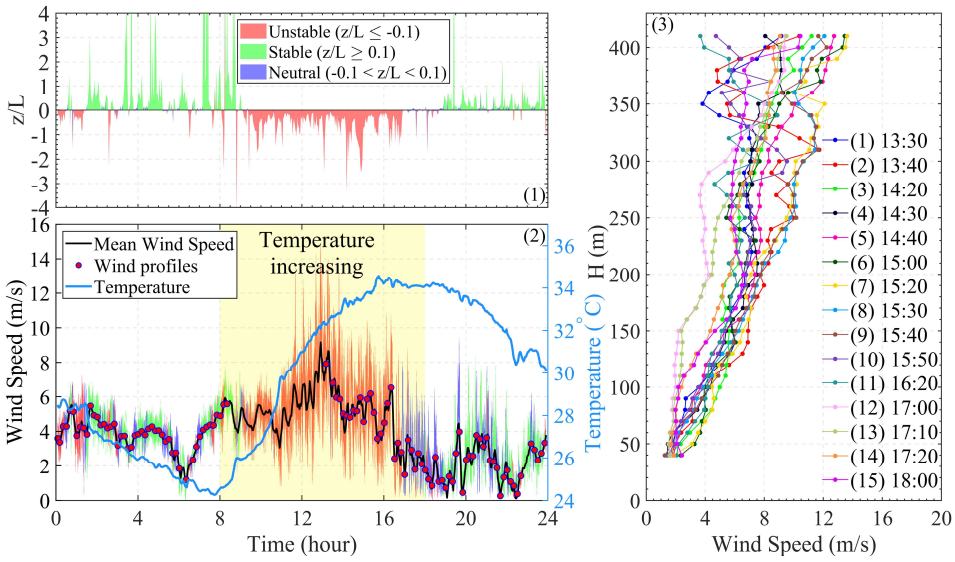

(b) Event2 (June 9, 2017)

Fig. 4 Typical time history of wind events and wind profiles

Fig. 4 shows that after sunrise (about 08:00), wind speed and air temperature rise concurrently, reaching peak values around 12:00 to 16:00, during which distinctly unstable stratification prevails. By about 18:00, the temperature begins to decline; wind speed drops first and then partially recovers after 22:00 as neutral and stable conditions develop, although the speeds remain below the afternoon values observed under unstable conditions. This pattern illustrates the case described in Section 1, where thermally driven diurnal circulation yields the co-occurrence of unstable conditions and high winds. At the microscale, the instability-induced suppression of the mean wind may still operate via enhanced vertical transport, yet intense winds are already established at the structural site. Therefore, the empirical assumption that instability necessarily suppresses the mean wind becomes inadequate for complex mountainous terrain, underscoring the need for a new stability-corrected wind profile model.

3 Extraction of turbulent fluctuations and determination of atmospheric stability

The development of a stability-based wind profile correction model requires accurate extraction of turbulent fluctuations and reliable determination of atmospheric stability. Therefore, this section will determine the method for extracting fluctuations and examine the coherent transport between heat flux and turbulence.

(1) Coordinate system transform

To obtain physically meaningful turbulent fluctuations and reduce contamination from terrain-induced directional biases, the sonic measurements in the instrument-fixed (body-axis) frame are rotated into the wind-axis coordinate system. Fig. 5 illustrates the geometric relationship between these two frames. The grey solid arrows denote the north–south, east–west, and vertical body axes. The red solid vector represents the three-dimensional mean-wind direction, while the blue solid arrows indicate its projections onto the horizontal and vertical planes; the blue dashed segment outlines the horizontal plane. The black dashed arrows depict the rotated wind-axis frame in which the longitudinal component u aligns with the mean-wind vector, and the v-w components represent the lateral and vertical turbulent motions orthogonal to it.

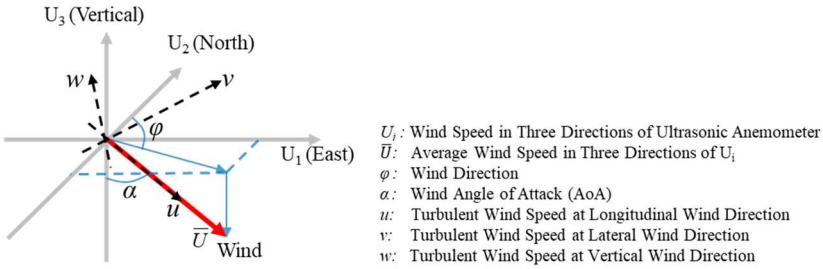

Fig. 5 Transformation from instrument coordinates to the wind-axis coordinate system

As seen in Fig. 5, aligning the coordinate system with the mean-wind direction ensures that the turbulent components are defined relative to the physically relevant flow axis rather than the instrument orientation, which may be influenced by local terrain and mast geometry. This transformation is essential for subsequent analyses, such as nonstationary decomposition, friction-velocity estimation, and heat-flux computation, because it eliminates cross-component correlations that would otherwise arise in the body-axis frame. The direction cosines required for this rotation are calculated using Eq.(5) to Eq.(7), based on the three-dimensional mean-wind vector.

$$\left(\cos\alpha_u,\cos\beta_u,\cos\gamma_u\right)=\frac{\left(\overline{U}_x,\overline{U}_y,\overline{U}_z\right)}{\overline{U}} \tag{5}$$

$$\left(\cos\alpha_v,\cos\beta_v,\cos\gamma_v\right)=\frac{(0,0,1)\times\left(\cos\alpha_u,\cos\beta_u,\cos\gamma_u\right)}{\left|(0,0,1)\times\left(\cos\alpha_u,\cos\beta_u,\cos\gamma_u\right)\right|}=\frac{\left(-\cos\beta_u,\cos\alpha_u,0\right)}{\sqrt{\cos^2\alpha_u+\cos^2\beta_u}} \tag{6}$$

$$\begin{aligned}\left(\cos\alpha_w,\cos\beta_w,\cos\gamma_w\right)&=\frac{\left(\cos\alpha_u,\cos\beta_u,\cos\gamma_u\right)\times\left(\cos\alpha_v,\cos\beta_v,\cos\gamma_v\right)}{\left|\left(\cos\alpha_u,\cos\beta_u,\cos\gamma_u\right)\times\left(\cos\alpha_v,\cos\beta_v,\cos\gamma_v\right)\right|}\\&=\frac{\left(-\cos\alpha_u\cos\gamma_u,-\cos\beta_u\cos\gamma_u,\cos^2\alpha_u+\cos^2\beta_u\right)}{\sqrt{\cos^2\alpha_u+\cos^2\beta_u}}\end{aligned} \tag{7}$$

Based on the direction cosines described above, the three-dimensional wind velocity components in the wind axis were obtained using Eq.(8).

$$\begin{aligned}U_u(t)&=U_x(t)\cos\alpha_u+U_y(t)\cos\beta_u+U_z(t)\cos\gamma_u\\U_v(t)&=U_x(t)\cos\alpha_v+U_y(t)\cos\beta_v+U_z(t)\cos\gamma_w\\U_w(t)&=U_x(t)\cos\alpha_w+U_y(t)\cos\beta_w+U_z(t)\cos\gamma_w\end{aligned} \tag{8}$$

where $U_u(t)$, $U_v(t)$, and $U_w(t)$ denote the time series of wind velocity along the wind axis in the longitudinal, lateral, and vertical directions.

(2) Stationary test

The run test method [57, 63] is used to assess time-series stationarity, evaluating the signal via the test statistic z.

$$z = \frac{r - E(r)}{\sigma(r)} \tag{9}$$

$$\begin{cases} E(r) = \dfrac{2n_1 n_0}{n_1 + n_0} + 1 \\ \sigma(r) = \sqrt{\dfrac{2n_1 n_0 \left(n_1 + n_0\right)}{\left(n_1 + n_0\right)^2 \left(n_1 + n_0 - 1\right)}} \end{cases} \tag{10}$$

where $E(r)$ and $\sigma(r)$ are the mean value and standard deviation of r, for a fluctuating series x_t (5 minutes), choose the sample median as the reference. Encode each point as positive if x_t is above the reference and negative if below. Let n_1 and n_0 be the counts of positive and negative, and let r be the number of runs (maximal consecutive identical signs). Then, evaluate the test statistic z. The null hypothesis is that the sample is stationary. If $|z| \geq 1.96$ (p-value<0.05), reject the null hypothesis and classify the signal as nonstationary. Stationarity is evaluated for each 5-minute window, and the nonstationarity ratio is the proportion of windows deemed nonstationary in the original signal.

3.1 Decomposition model

Accurate separation of trend and fluctuations in mountainous wind fields requires selecting an appropriate decomposition model. Application needs differ [49]: extreme-wind analyses demand precise trend extraction, whereas spectral and flux computations require strictly stationary fluctuations. Because complex-terrain winds are strongly nonstationary, event-prone, thermally mixed, and structurally complex, the model must satisfy trend-fidelity and stationarity requirements [64].

3.1.1 Stationary method

The stationary method is first introduced, in which the commonly used wind speed model within the stationary boundary layer (SBL) is expressed in Eq.(11). This model employs a fixed time window to calculate mean values and is directly associated with the wind axis transformation defined in Eq.(5) to Eq.(8).

$$\begin{cases} U_u(t) = \bar{U} + u(t) \\ U_v(t) = v(t) \\ U_w(t) = w(t) \\ T(t) = \bar{T} + T_f(t) \end{cases} \tag{11}$$

where $\bar{U}$ and $\bar{T}$ denote the mean wind speed and temperature within each time window, $u(t)$, $v(t)$, $w(t)$, and $T_f(t)$ denote the time series of fluctuating components in the longitudinal, lateral, vertical

246 directions and temperature within each time window.

247 *3.1.2 Nonstationary method*

248 Unlike the stationary wind speed model, the nonstationary method directly decomposes the
249 time series into a time-varying mean component and the corresponding fluctuation component, as
250 shown in Eq.(12).

$$\begin{cases} U_u(t) = \bar{U}_u^*(t) + u^*(t) \\ U_v(t) = \bar{U}_v^*(t) + v^*(t) \\ U_w(t) = \bar{U}_w^*(t) + w^*(t) \\ T(t) = \bar{T}^*(t) + T_f{}^*(t) \end{cases} \tag{12}$$

251 where $\bar{U}^*(t)$, $\bar{V}^*(t)$, $\bar{W}^*(t)$, $\bar{T}^*(t)$ represent the time-varying mean component, while $u^*(t)$, $v^*(t)$,
252 $w^*(t)$, $T_f^*(t)$ denote the stationary fluctuating components obtained using the nonstationary model.
253 In this study, both the moving average method and the discrete wavelet transform (DWT) are
254 employed for comparative analysis.

255 (1) Moving Average Method

256 The moving average method is one of the most straightforward and widely used approaches
257 for constructing time-varying mean wind, and it has been applied across various research contexts.
258 This method is based on a classical assumption: by selecting an appropriately sized time window,
259 the averaging process can effectively filter out low-frequency components or trend signals.

$$\bar{U}(z,t) = \frac{1}{T_0}\int_{t-T_0/2}^{t+T_0/2} U(z,t)dt \tag{13}$$

260 where the time-varying mean wind $\bar{U}(z,t)$ is determined using a moving average (MA) over a
261 short time interval T_0.

262 (2) Discrete Wavelet Transform

263 In the discrete wavelet transform (DWT), many wavelet bases—such as the Daubechies
264 family—possess compact support in function space [65], which minimizes frequency leakage and
265 modal mixing during decomposition, ensures strong local orthogonality and spectral independence
266 among decomposed components. Orthogonal DWT expands $x(t)$ on the scaling $\varphi(t)$ and wavelet $\zeta(t)$
267 (Eq.(14)). The $\varphi(t)$ encodes the low-frequency trend and the $\zeta(t)$ encodes the multiscale fluctuations.
268 $\zeta(t)$ follows from $\varphi(t)$ via high-pass coefficients g_k (Eq.(15)), and dilation and translation yield $\zeta_{j,k}(t)$
269 (Eq.(16)).

$$x(t) = \sum_{k} a_{m,k}\varphi_{m,k}(t) + \sum_{j=1}^{m}\sum_{k} b_{j,k}\zeta_{j,k}(t) \tag{14}$$

$$\zeta(t) = \sum_{k} g_k \varphi(2t-k) \tag{15}$$

$$\zeta_{j,k}(t) = 2^{j/2}\zeta\left(2^j t - k\right) \tag{16}$$

where m denotes the number of decomposition levels, and k represents the time index associated with the location of the mother wavelet in the time series during the DWT process. The coefficients $a_{m,k}$, $b_{j,k}$ correspond to the low-frequency (trend) and high-frequency (detail) components at the m^{th} and j^{th} levels, respectively. The $\varphi(t)$ and $\zeta(t)$ are the basis functions associated with the selected wavelet family, such as db10 from the Daubechies wavelet series. The cutoff frequency and the equivalent window length [49] for each decomposition level are calculated as follows:

$$\begin{aligned} f_j &= \log_2(f_s \times 2^j) \\ d_j &= \left(\frac{f_s}{2^{j+1}}\right)^{-1} / 2 \end{aligned} \tag{17}$$

where f_s denotes the sampling frequency of the signal, and j represents the corresponding decomposition level.

3.2 Determination of the turbulent wind decomposition method

3.2.1 Determination of wind speed decomposition model

(1) Stationary method

In the stationary model, window length controls fluctuation extraction because it changes the mean wind in the body coordinate system used for the wind-axis transformation (Eqs. (5)–(8)), thereby altering the direction-cosine matrix. Time series of three-component wind speeds (longitudinal, lateral, vertical) and temperature collected from May 1 to June 30, 2017 were analyzed using ten window lengths (30–1 min) to extract turbulent fluctuations. Stationarity was tested at each window length, and the proportion of stationary segments is summarized in Fig. 6.

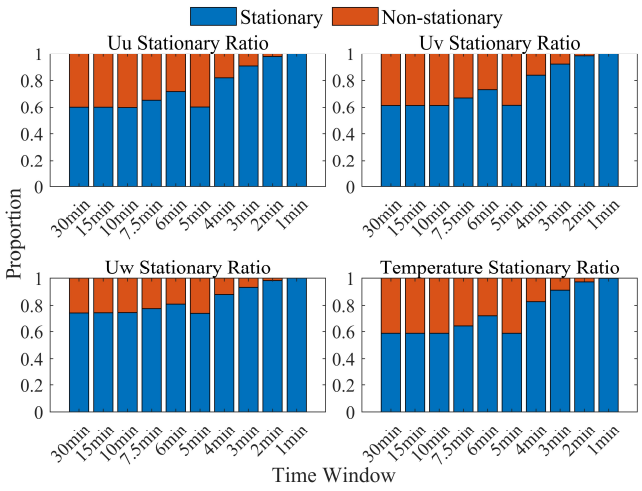

Fig. 6 Stationarity testing of fluctuating samples obtained using different time window lengths

As shown in Fig. 6, the proportion of stationary samples rises as the window shortens, and signals are fully stationary below 2 minutes. However, short windows induce frequent mean changes in the wind-axis transform and conflict with 10-minute mean profiles. 1–2-minute windows can truncate 100–200-second wind events (such as gusts or thunderstorm outflows), missing their full evolution. These issues indicate that fixed-window stationary models are inadequate in complex mountainous terrain, and nonstationary methods are more effective in such environments.

(2) Nonstationary method

A typical strong wind event was selected from 14:00 to 16:00 on May 2, 2017. The same turbulent-wind signal was decomposed with sliding intervals of 300–10 s and DWT levels 12–4 using the Daubechies-10 (db10) basis, followed by previous studies [66]. Fig. 7 (a1) and (b1) show the relationship between the original signal and the time-varying mean (trend) extracted with the MA (a1) and DWT (b1) methods using three representative window lengths T_0 (MA) and equivalent windows d (DWT). Fig. 7 (a2) and (b2) present the stationarity tests for the longitudinal component U_u.

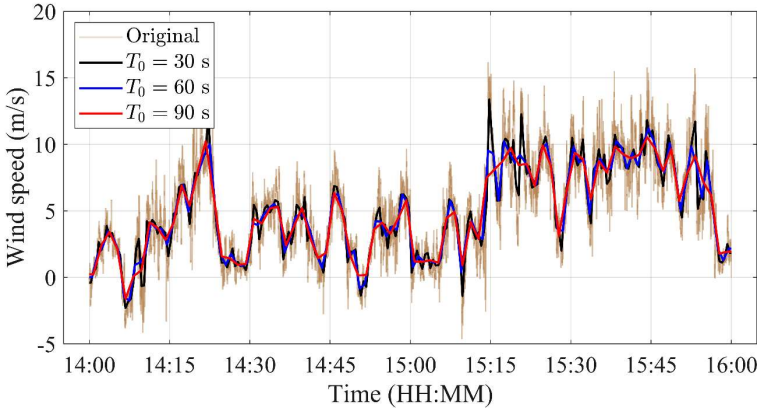

(a1) Time-varying mean wind obtained using the MA method

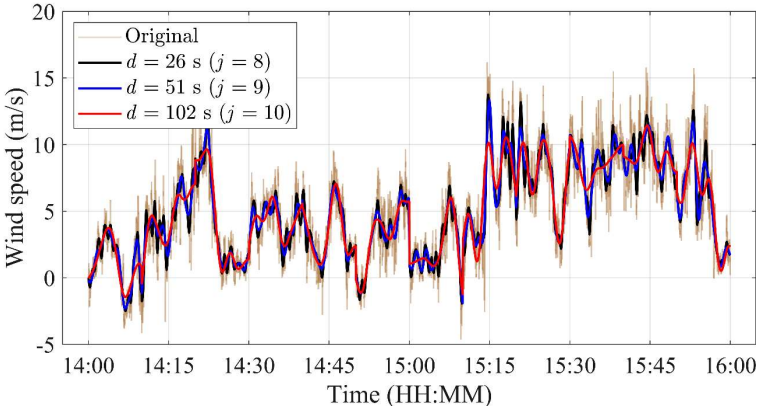

(a2) Time-varying mean wind obtained using the DWT method

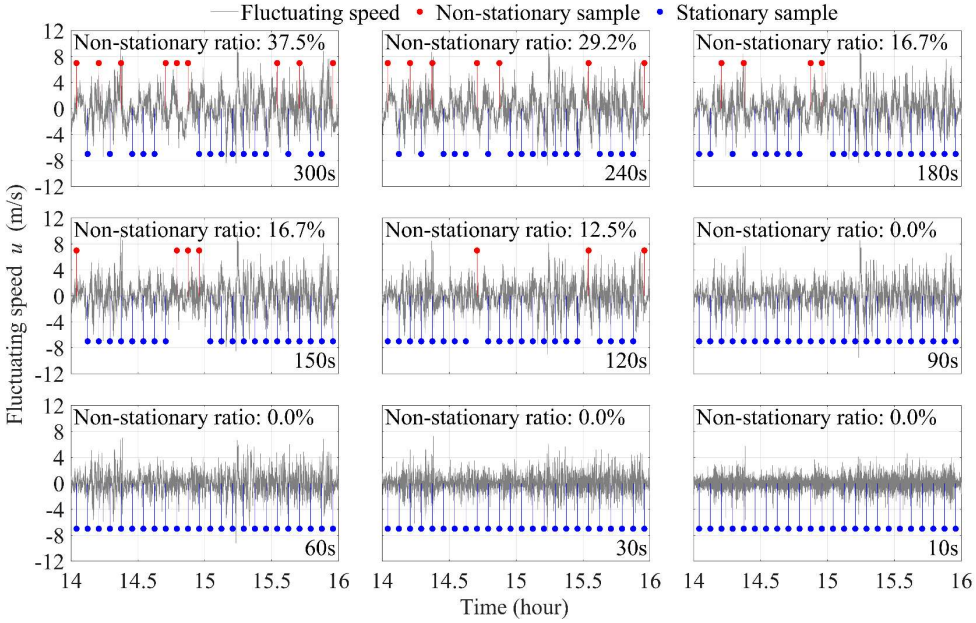

(b1) Fluctuating wind component extracted using the MA method

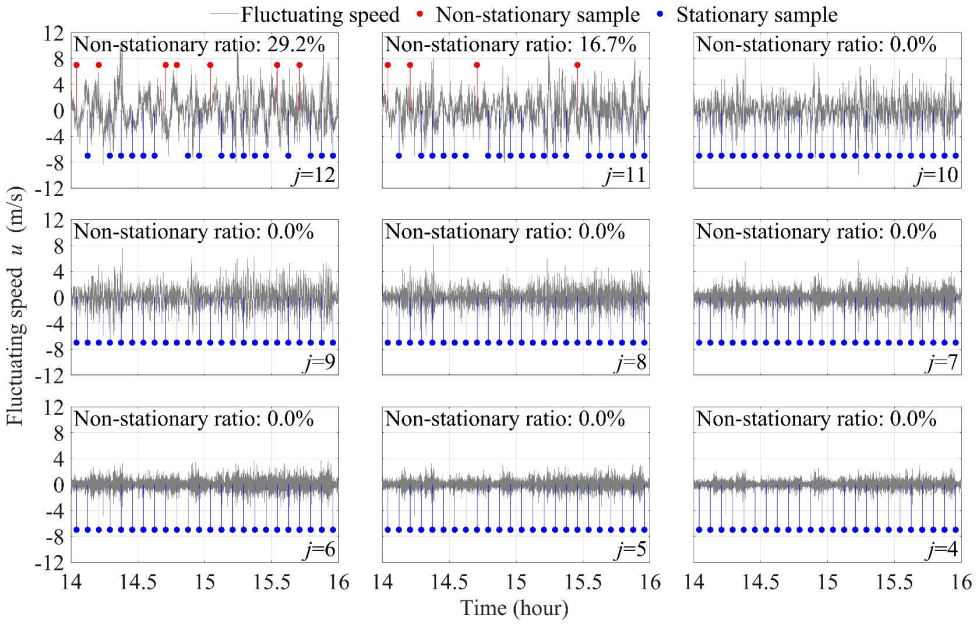

(b2) Fluctuating wind component extracted using the DWT method

Fig. 7 Decomposition of a representative nonstationary wind event using MA and DWT methods

As shown in Fig. 7, full stationarity of the fluctuating wind is achieved when the moving average window reaches 90 seconds, or the wavelet decomposition level reaches 10 (equivalent to a 102-second window). Both MA and DWT can remove the time-varying mean wind; however, it remains unclear whether this removal fully eliminates large-scale inflow trends while ensuring stationarity and meeting the requirements for reconstructing small-scale turbulence. We therefore further examine the structure of the extracted signals to assess their adequacy.

3.2.2 Selection of decomposition method and decomposition level

Two metrics are used to compare decomposition methods: correlation and turbulent kinetic energy (TKE) [10, 67]. The correlation test assumes that residual trend leaves dependence between the time-varying mean wind and the extracted fluctuations, so coefficients closer to zero indicate more complete trend removal. The TKE test evaluates spectral energy across scales: lower frequencies reflect large-scale motions, higher frequencies smaller eddies, and the dominant energy-containing band identifies the turbulent component [68]. Abrupt TKE shifts across scales can indicate a clean separation of trend from fluctuations [66]. To address nonstationarity in complex terrain, evolutionary power spectral density (EPSD) is used to resolve the time-varying spectrum [69].

To assess the ability of different nonstationary decomposition methods to separate low-frequency trend components from turbulent fluctuations, the correlation between the time-varying mean and the corresponding fluctuation components (longitudinal, lateral, vertical wind speed, and temperature) is evaluated using both the moving-average (MA) method and the discrete wavelet transform (DWT). Fig. 8 summarizes these correlations across a range of MA window lengths (10–200 s) and DWT decomposition levels (4–11), where lower correlation values indicate a more effective separation between the trend and fluctuating components.

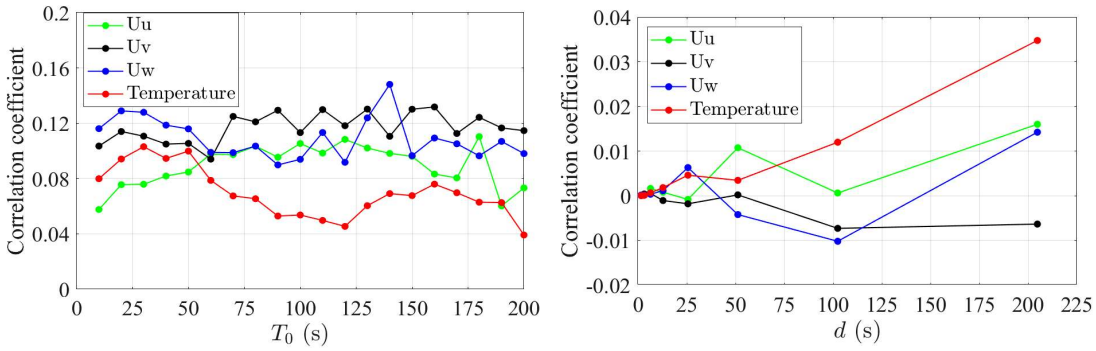

(a) MA method: correlation across window lengths (10–200 s)

(b) DWT method: correlation across decomposition levels (4–11)

Fig. 8 Correlation between the time-varying mean component and the turbulent fluctuation extracted using nonstationary decomposition methods

As shown in Fig. 8, the MA method yields correlation coefficients consistently above 0.04 for all components when the sliding interval is shorter than 200 s, indicating that residual low-frequency trends remain in the fluctuation signal. In contrast, the DWT-based decomposition produces correlation values below 0.04 across a wide range of scales, and the correlation approaches zero when the decomposition level corresponds to time scales shorter than approximately 100 s. These results demonstrate that the DWT provides a cleaner and more physically consistent separation between the mean and turbulent components, supporting its use for nonstationary decomposition in complex-terrain wind environments.

The longitudinal turbulent wind components extracted at different decomposition scales, shown in Fig. 7, were analyzed using EPSD, following Priestley's evolutionary spectrum method [70]. The time-varying spectral content of the stochastic process X_t is estimated using a localized Fourier transform of the form:

$$U_x(\omega,t)=\int_{t-\mathrm{T}}^{t} g(u)X_{t-u}\mathrm{e}^{-\mathrm{i}\omega(t-u)}\mathrm{d}u \tag{18}$$

$$g(u)=\begin{cases}\dfrac{1}{2\sqrt{h\pi}} & (|u|\le h)\\ 0 & (|u|>h)\end{cases} \tag{19}$$

where $g(u)$ is a time-domain window function, this formulation enables the characterization of spectral evolution by extracting frequency information around each time instant. The use of the window function effectively limits the contribution of distant samples, introducing a smoothing effect in the frequency domain. The squared modulus of the filtered result $|U_x(\omega,t)|^2$ is weighted-averaged within the neighborhood of time t using a specific window function, yielding the local

power spectral density (PSD) estimate at frequency ω:

$$\hat{S}_x(\omega,t)=\int_{-\infty}^{\infty} W_{\mathrm{T}'}(v)\left|U_x(\omega,t-v)\right|^2\,\mathrm{d}u \tag{20}$$

$$W_{T'}(t)=\begin{cases}\dfrac{1}{\mathrm{T}'} & \left(|t|\le\dfrac{1}{2}\mathrm{T}'\right)\\ 0 & \left(|t|>\dfrac{1}{2}\mathrm{T}'\right)\end{cases} \tag{21}$$

where $S(\omega,t)$ represents the estimated evolution power spectral density (EPSD) of X_i; $W_{T'}(t)$ is the weighting function proposed in this study; T' denotes the effective time width of $W_{T'}(t)$ (in seconds). Following previous studies [10, 57] on spectral resolution in time-frequency analysis, the parameter h in Eq.(19) is set as $7/\Delta\mathrm{T}=70$, where ΔT is the sampling interval of 0.1s. The effective time width, T', is set to 256s.

To examine how different nonstationary decomposition methods represent the time–frequency characteristics of turbulent motions, the EPSD is computed for fluctuation components obtained using both the MA method and the DWT. The EPSD provides a localized spectral representation of energy distribution across time and frequency, allowing the identification of leakage, scale mixing, and the clarity of multiscale turbulent structures. Fig. 9 compares the EPSD patterns generated by the two methods across representative decomposition scales.

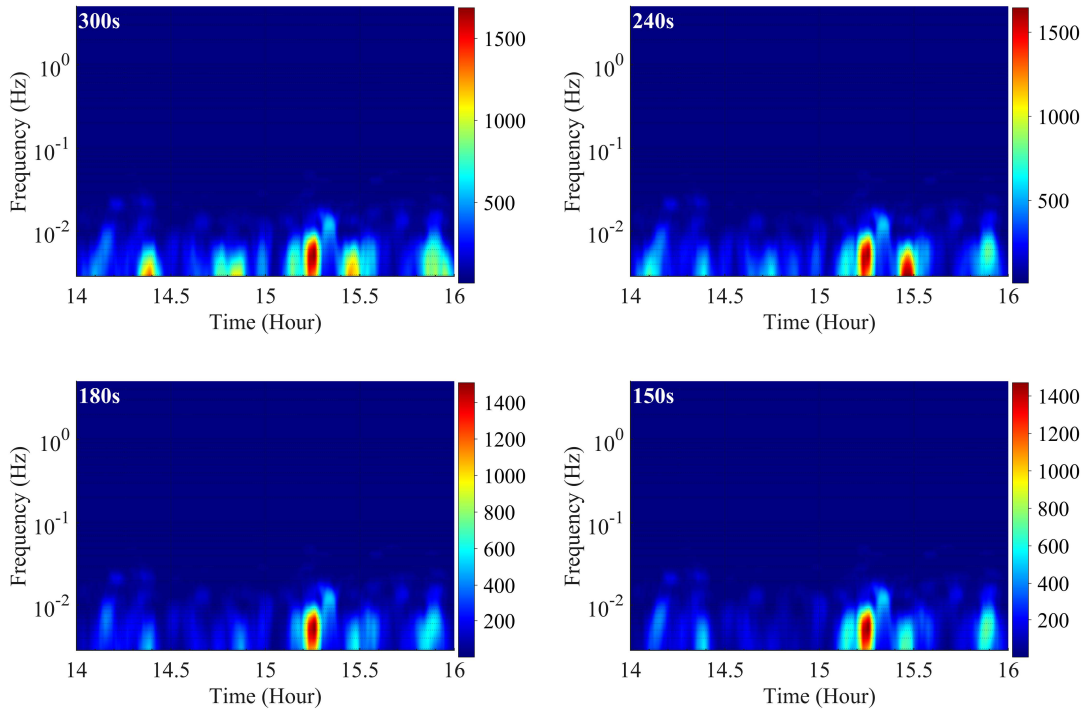

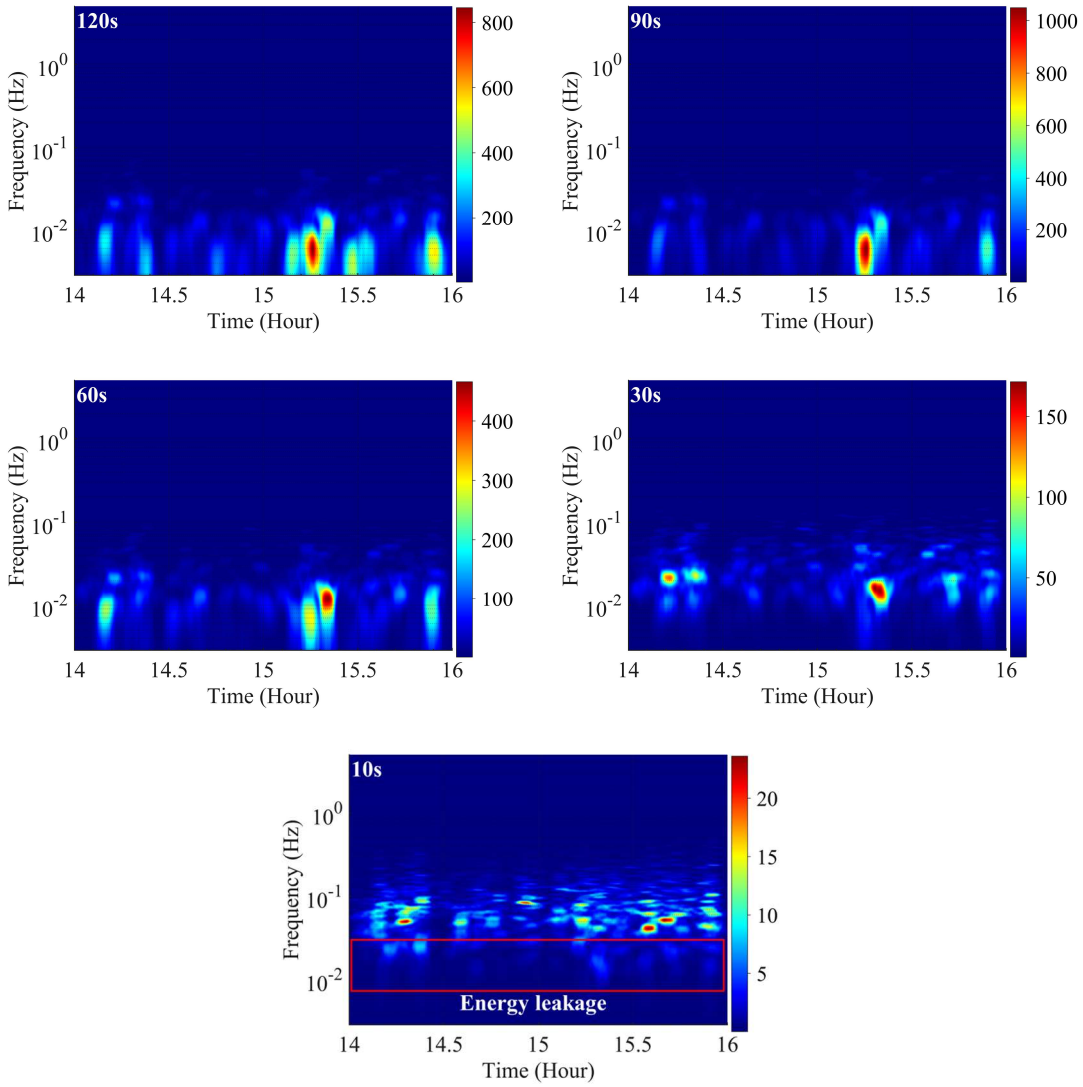

(a) EPSD obtained using MA method at representative window lengths

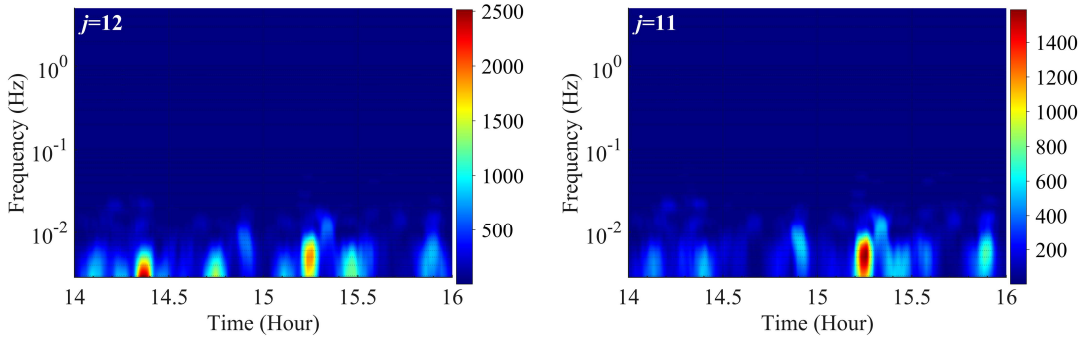

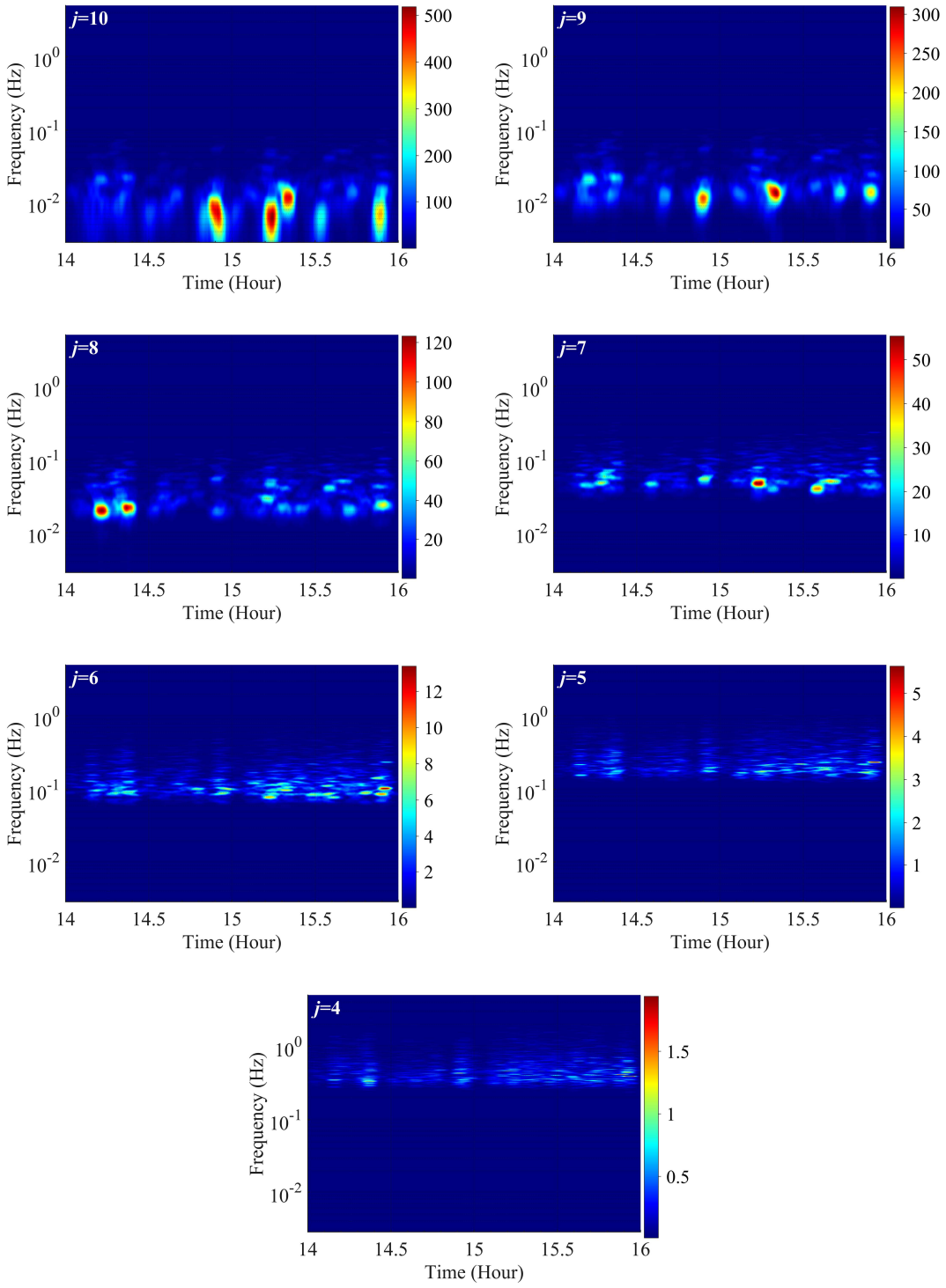

(b) EPSD obtained using DWT at representative decomposition levels

Fig. 9 EPSD of turbulent wind fluctuations extracted using nonstationary decomposition methods

As illustrated in Fig. 9, the MA method exhibits persistent bright bands in the low-frequency region, even when short window lengths are applied, indicating incomplete removal of large-scale trends and consequent spectral leakage. This leakage blurs the separation among turbulent scales

and results in mixed-frequency structures that do not reflect the underlying physics. In contrast, the DWT suppresses these low-frequency components more effectively, producing EPSD patterns with distinct and well-resolved multiscale features. This clearer separation of energy across frequencies demonstrates that wavelet-based decomposition is better suited for representing nonstationary turbulence and underpins the later selection of DWT as the primary detrending method.

The selection of decomposition levels for turbulent wind must be guided by the specific research objectives. For flux estimation and spectral modelling, it is critical to identify the cutoff frequency of the trend component to prevent contamination of the turbulent signal by large-scale trends. This identification is typically done by spotting abrupt changes in energy content across decomposition levels. Further inspection of the EPSD results in Fig. 9 reveals that decomposition levels 10 and 8 both show more than a 50% reduction in spectral energy relative to the previous level. Prior studies [36, 49, 71] indicate that to capture the turbulent characteristics of rapidly evolving nonstationary strong-wind events (e.g., thunderstorm winds), the analysis window should satisfy stationarity requirements and exceed the duration of the event's intense gusts. For short-lived strong-wind conditions, a window of approximately 30 seconds to 2 minutes is recommended [71]. With the 10 Hz sampling used here, the equivalent window computed from the governing relation $d_j = (\frac{f_s}{2^{j+1}})^{-1} / 2$ maps to wavelet levels with characteristic duration d≥26s; here, they are level 8 and higher. Given the coexistence of nonstationarity and localized intense wind events in complex mountainous terrain, level 10—corresponding to a relatively large equivalent time window (104s)—was reasonably selected as the target decomposition level.

3.3 Determination of flux transport

In the troposphere, vertical heat transport is governed by vertical turbulence; however, it is not straightforward to determine how eddies of different sizes (with large eddies concentrating energy at lower frequencies and small eddies at higher frequencies) convey thermal fluctuations of different scales. Unlike the stationary models, the use of nonstationary models extracts low-frequency, large-scale motions as part of the time-varying mean. In such cases, it is essential to first determine whether the transport of physical quantities such as heat or atmospheric pollutants is primarily governed by small-scale high-frequency turbulent eddies or by large-scale low-frequency motions

associated with the time-varying mean flow. Therefore, flux transport should not be determined solely based on energy content, but rather by identifying the coupled variability between the transported scalar and the corresponding turbulent fluctuations, with particular emphasis on transitions in effective transport.

Meanwhile, multiscale decompositions such as DWT, EMD, and VMD partition a signal into components characterized by intrinsic time scales; each decomposition level can be associated with a center frequency and an effective bandwidth (or an equivalent cutoff interval). Consequently, these decompositions do not necessarily preserve identical scale partitions across different variables (e.g., vertical velocity and temperature). To quantify the coupling between variables, the cospectrum is introduced (Eq.(22)) to quantify this scale-by-scale transport on a frequency-by-frequency basis. The cospectrum is defined as the real part of the cross-spectrum between two fluctuating signals [73]. It reflects the degree of coupled transport between the two variables across different frequencies, where the frequency indicates the characteristic scale of turbulent eddies, and the amplitude represents the intensity of scalar transport (e.g., heat) at that scale [74]. The cospectrum reflects the coherence between two fluctuating variables, and its integral (Eq.(23)) represents the cumulative flux contribution across the frequency domain [75]. Therefore, the cospectrum density provides a direct measure of flux contributions across different frequency bands.

$$C_{wT}(f) = \mathrm{Re}\{S_{w(t)}(f) S_{T_f(t)}(f)\} \tag{22}$$

$$H_*(f) = \int C_{wT}(f)\mathrm{d}f \tag{23}$$

where f denotes the frequency.

To investigate the coupled transport across scales, the cospectrum of sensible heat flux was computed under different decomposition levels of turbulent wind. By retaining different frequency components in the decomposed wind and temperature signals, the resulting cospectrum reveals the corresponding scale-dependent coupling behavior. In Fig. 10, j denotes the discrete wavelet decomposition level applied to the vertical wind component used in the cospectrum calculation. Within each subfigure, spectral lines of different colours represent varying decomposition levels k applied to the temperature fluctuations. The cumulative cospectrum provides further insight into the contribution of each scale combination to the total flux.

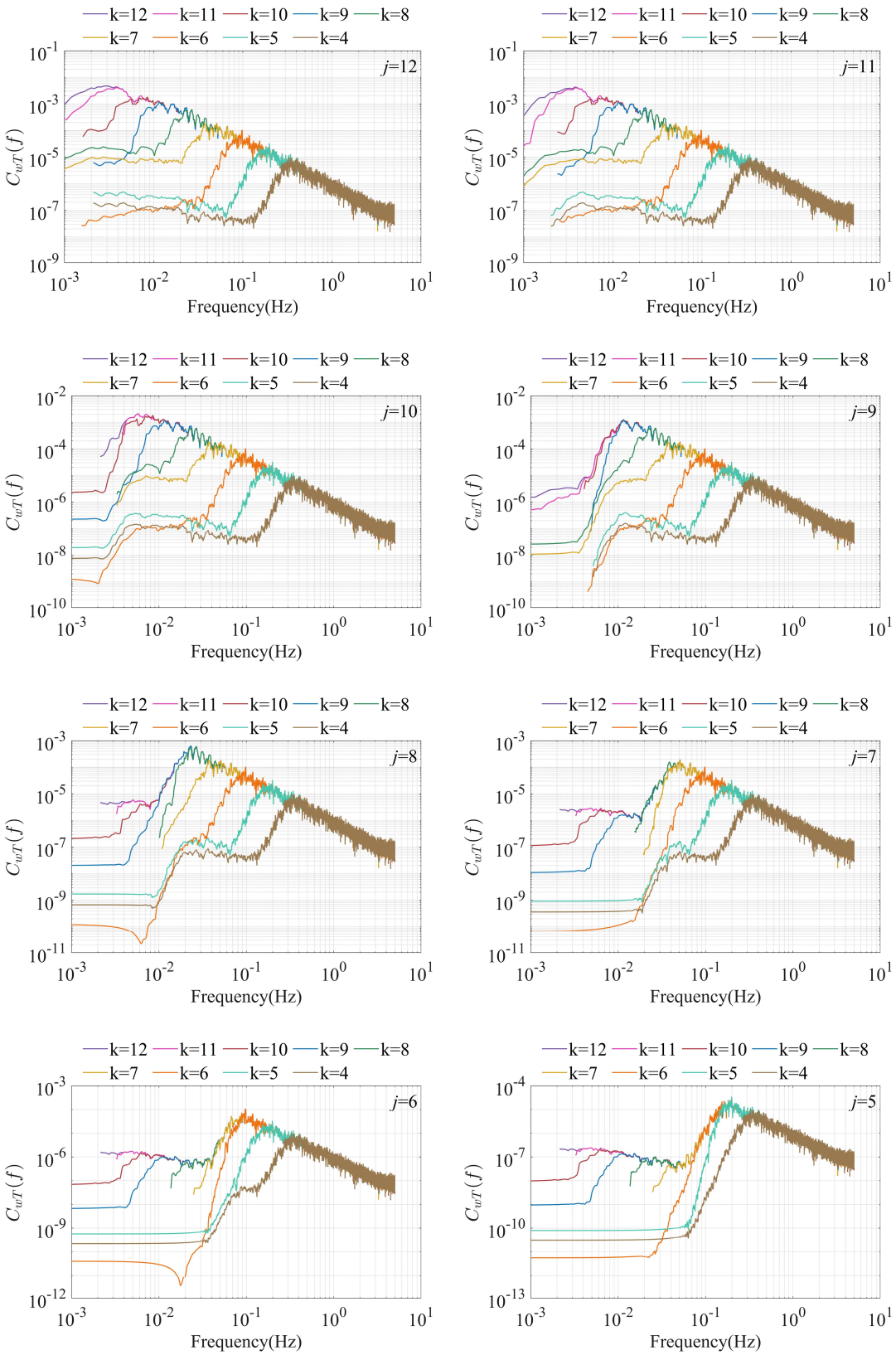
k=12 k=11 k=10 k=9 k=8
k=7 k=6 k=5 k=4
j=12
j=11
j=10
j=9
j=8
j=7
j=6
j=5
$C_{wT}(f)$
Frequency(Hz)

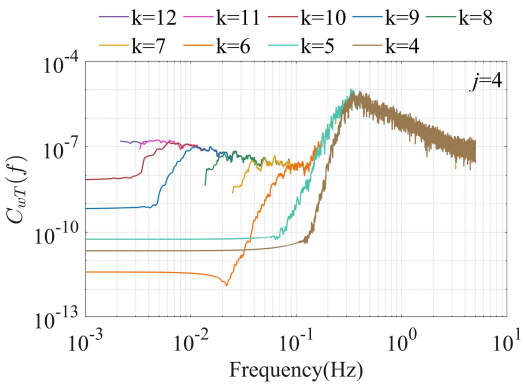

(a) Cospectrum of heat flux

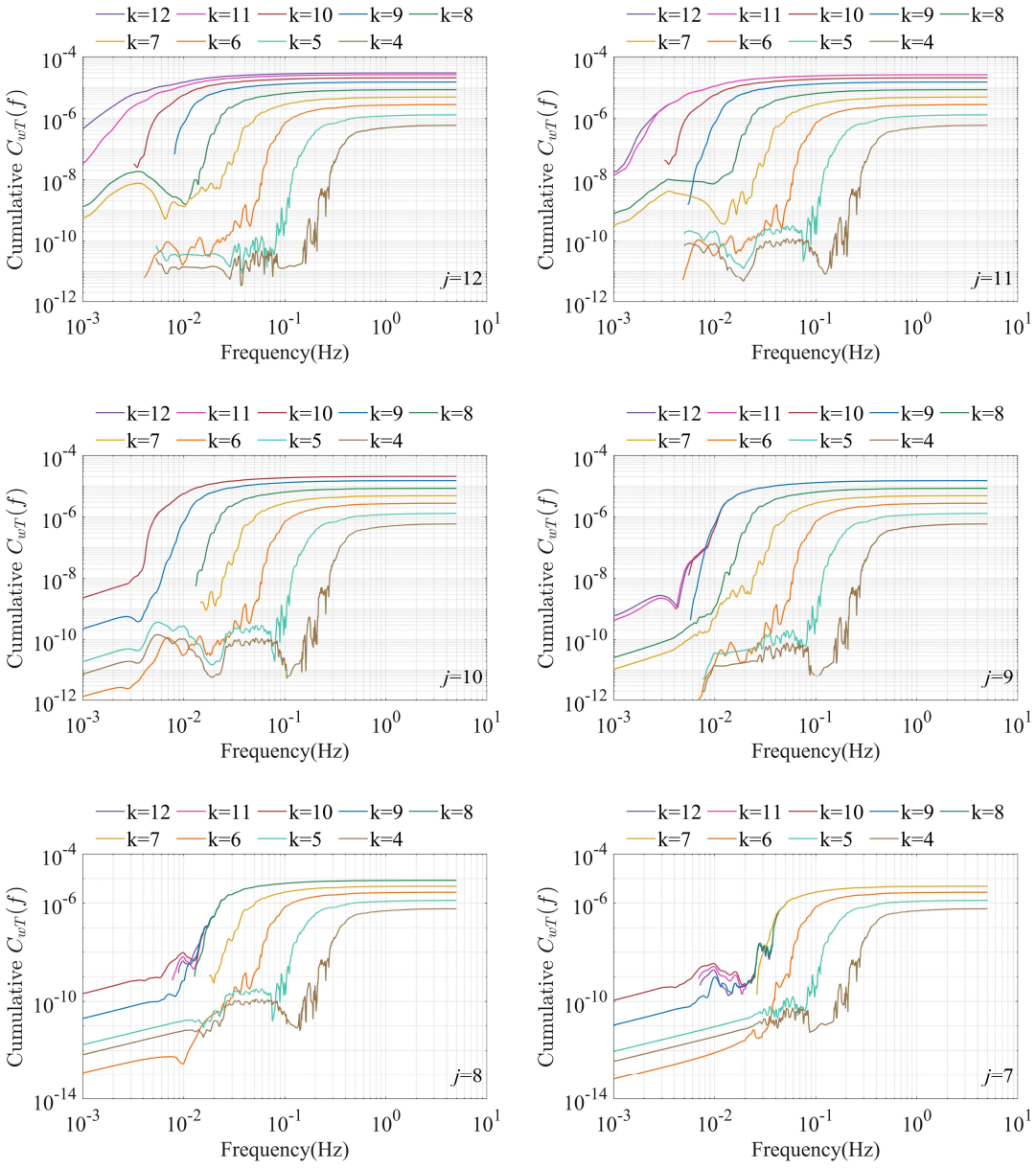

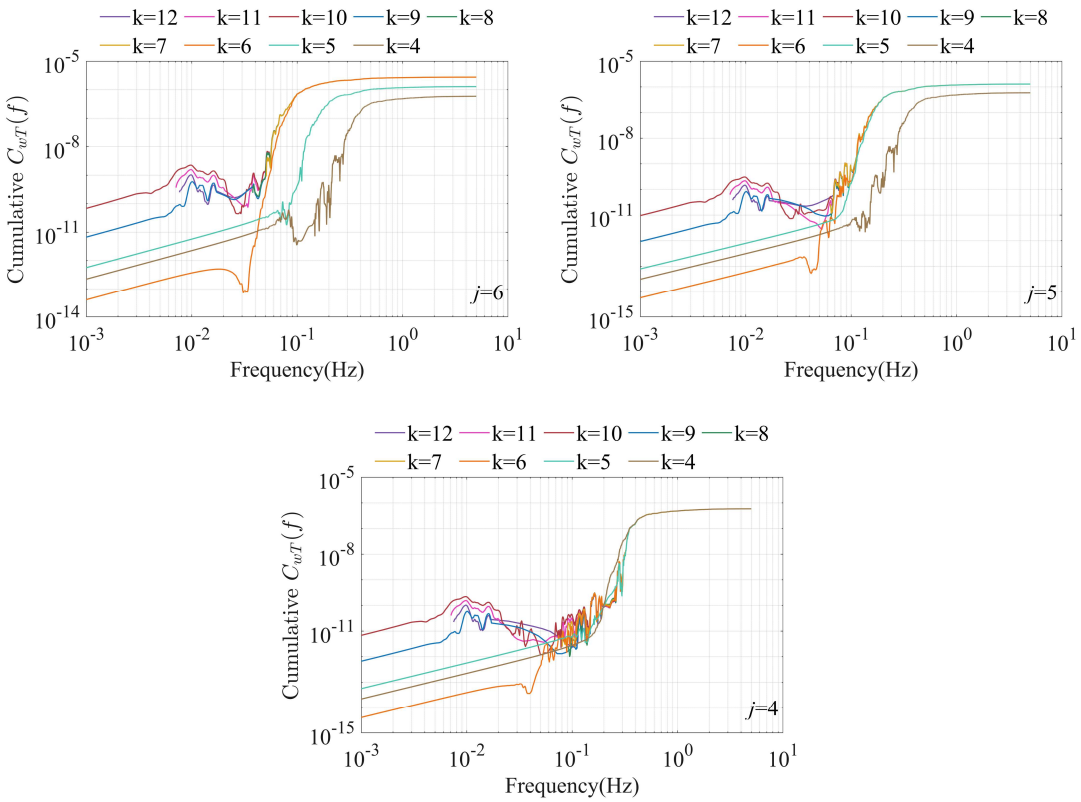

(b) Cumulative cospectrum of heat flux

Fig. 10 Heat-flux transport characteristics under different DWT decomposition levels of vertical wind and temperature

Because the cospectra are plotted on logarithmic axes, Fig. 10a shows only the positive portions of the scale-by-scale heat-flux contributions; negative values occurring in some frequency bands are fully retained in the integrated flux shown in Fig. 10b. The cumulative cospectra exhibit pronounced spectral-line overlap, indicating that beyond a certain scale, additional high-frequency temperature components contribute negligibly to the total flux. This behavior is consistent across different wind events, wind-profile types, and stability regimes, as further illustrated in Appendix Fig. A2.

The convergence of the cumulative curves demonstrates that the integrated flux becomes essentially insensitive to the choice of temperature decomposition level once the dominant flux-carrying scales are included. For instance, when the vertical-wind decomposition level is varied from j = 11 to j = 8, the uppermost cumulative curves successively correspond to k = 11, 10, 9, and 8, yet the curves nearly coincide. This strong overlap confirms that meaningful heat-flux transport is concentrated within a limited frequency band and that decomposition levels beyond this band have no substantive impact on flux estimation. This convergence property provides a practical

criterion for selecting temperature and wind decomposition levels when applying DWT-based flux estimation in nonstationary mountainous winds.

Since both the wind-speed and temperature series were detrended using wavelet decomposition, selecting an unduly low decomposition level (i.e., a cutoff that is too high and too broad) removes the low-frequency content from both signals, leaving little or no power in the low-frequency band, which leads to sharp drops in the figure. This circumstance can be addressed by constraining the analysis window and choosing decomposition levels whose characteristic window length is sufficiently long and aligned with the study objectives. The frequency band of the trend component should be determined with respect to the study objective and the analysis window. Prior study [49] indicates that, for strongly nonstationary intense-wind events, an equivalent window of approximately 30 seconds to 2 minutes is appropriate. Therefore, they are level 8 and higher. Consequently, cross-spectral comparisons that involve levels ≤ 7 (finer than level 8) are not physically informative for this purpose; they are shown only to illustrate the general phenomenon of cumulative cospectral overlap. For levels ≥ 8, both the spectra and the cumulative cospectra are smooth, the spectral-line overlap is evident, and the estimates are reliable.

Given that the integral of the cospectrum corresponds to the flux value, the observed convergence behavior suggests that, under a fixed decomposition level for the fluctuating wind, higher decomposition levels of temperature—despite containing more high-frequency energy—can no longer find corresponding “coherent partners” in the wind field for effective heat transport. Since vertical heat flux depends on the coherence between temperature and velocity fluctuations, once the frequency range represented by the temperature decomposition exceeds that of the wind, the excess high-frequency temperature components cease to contribute to coherent transport and instead behave as isolated disturbances. Therefore, the decomposition level of temperature should be truncated at the point where the cospectral curves begin to converge, ensuring a frequency range compatible with the wind fluctuations that actively participate in heat transport. Based on this criterion, level 9 is selected as the optimal decomposition level for temperature fluctuations.

3.4 Atmospheric stability estimation and dimensional analysis

Given that the Obukhov similarity theory and its main empirical functions were developed in earlier periods, the underlying fluctuating wind components were primarily extracted using

stationary models based on fixed time windows. To extend their applicability to modern nonstationary decomposition methods, it is necessary to compare the differences between stationary and nonstationary wind speed models in flux estimation and atmospheric stability calculations. In this study, Obukhov length was calculated using both the conventional 10-minute stationary model and wavelet-based nonstationary decomposition.

The normalized standard deviations of each fluctuating component were then compared. Fig. 11 depicts how the normalized standard deviations (σ/u_*, σ/θ_*) of wind components (u, v, w) and temperature (θ_* calculated by (24)) vary as a function of the stability parameter z/L.

$$\theta_* = -H_* / u_* \tag{24}$$

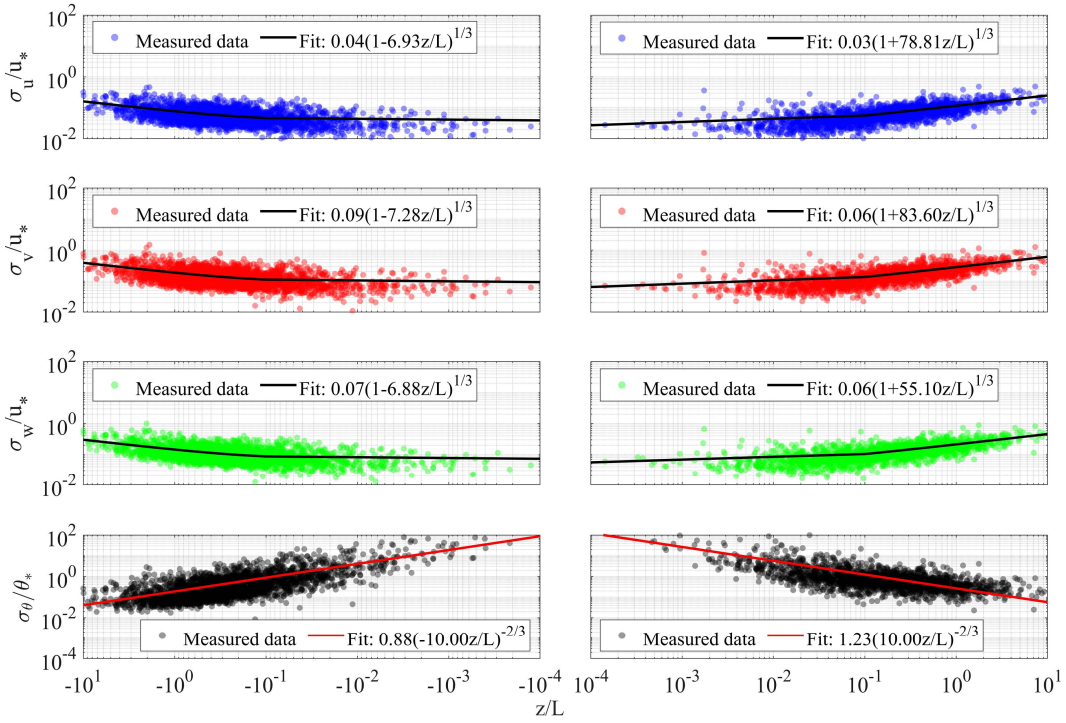

(a) Stationary method

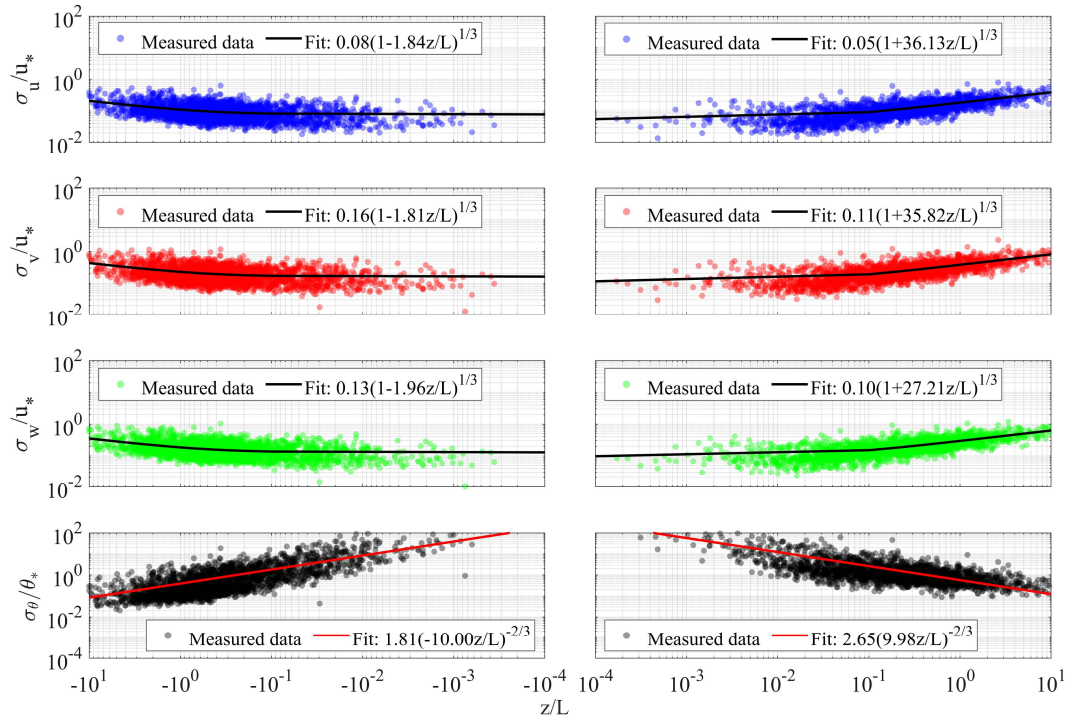

(b) Nonstationary method

Fig. 11 Normalized standard deviations of the velocity and temperature fluctuations versus the stability parameter z/L under stationary and nonstationary decomposition.

The results show that, regardless of atmospheric stratification, the normalized standard deviation of wind speed varies with *z/L* according to a 1/3-power law, a behavior that closely matches the dimensional-analysis prediction of the Monin–Obukhov similarity theory (MOST). Under MOST and Eq.(4), the ratio of friction velocity to a characteristic turbulence length scale is the principal controlling parameter, leading to the following dimensional relationship:

$$\sigma_u^2 \propto u_*^2 \left(\frac{z}{L}\right)^{2/3} \quad \Rightarrow \quad \frac{\sigma_u}{u_*} \propto \left(\frac{z}{L}\right)^{1/3}$$

This dimensional relationship has been validated by numerous theoretical and experimental studies [76-78] and represents a typical formulation of the Monin–Obukhov similarity theory, thereby providing a basis for verifying the constant-flux assumption. To further substantiate the general applicability of this relationship, we validated it across three independent seasonal datasets; see Fig. A1.

Analysis of measured data shows that the normalized temperature standard deviation σ_θ/θ^* exhibits a −2/3 power-law dependence on the stability parameter *z/L*, consistent with previous observational findings. This relationship is consistent with previous observational studies [79-80],

475 which reported a power-law dependence between normalized thermal fluctuations and *z/L*. The
476 corresponding dimensional relationship can be expressed as follows.

477 $$\frac{\sigma_\theta}{|\theta_*|} \propto \left(\frac{z}{L}\right)^{-2/3}$$

478 According to the formulation of atmospheric stability in Eq.(4), the heat flux appears in the
479 denominator, which implies that the negative exponent in the −2/3 power law is inevitable, and the
480 normalized temperature standard deviation is therefore proportional to the inverse of the stability
481 parameter raised to the 2/3 power. Dimensional analysis of the relationship between turbulent wind
482 and heat fluctuations with stability parameters reveals that the dimensional expression for
483 temperature fluctuations corresponds to the square of that for momentum fluctuations. This
484 relationship is in agreement with the classical Businger–Dyer relationships [81-82], which suggest
485 that the thermal universal function Φ_h is approximately equal to the square of the momentum
486 universal function Φ_m ($\Phi_h \approx \Phi_m^2$). It is worth noting that the Businger–Dyer relationships are derived
487 based on the assumption of similarity between momentum and heat transport ratios [17].

488 The power-law fitting results of wind speed and temperature, respectively, reflect the
489 dimensionally consistent momentum structure (first-order structure) and the statistical
490 characteristics associated with thermal transport (second-order structure) as described by Monin–
491 Obukhov similarity theory (MOST). These results provide strong support for the applicability of
492 MOST, even under complex terrain and nonstationary convective conditions, where consistent
493 scaling behavior is still maintained. This consistency confirms the reliability of atmospheric stability
494 estimations derived from nonstationary and cospectral methods for calculating wind and
495 temperature fluctuations. Considering the dimensional relationship between heat and momentum,
496 the subsequent refinement of the stability-corrected wind profile model will be developed based on
497 the Businger–Dyer relationship.

498 **4 Stability-corrected wind profile model for complex mountainous terrain**

499 For the study of turbulence characteristics over complex turbulent exchange surfaces, it is
500 generally accepted that observations from multiple measurement sites are required for validation
501 and confirmation [83]. Due to site limitations in actual field measurements, this study is based on

data from only a single measurement site and derives a correction function model based on atmospheric stability, specifically designed for complex mountainous terrain.

Wind profile patterns in mountainous terrain are shaped by complex topography, leading to variations in the evolution of wind parameters, which may weaken the applicability assumptions of the MOST correction framework—near-surface homogeneity, quasi-stationarity, constant-flux conditions, and weak horizontal gradients. In this study, the assumptions of stationarity and constant flux are addressed by nonstationary decomposition and verified using the normalized second-order statistics shown in Fig. 11. The weak-horizontal-gradients and near-surface homogeneity assumption is enforced through dataset screening.

To isolate wind-profile regimes suitable for MOST-based stability correction, all measured profiles were classified using a Self-Organizing Map (SOM) following Yan et al. [84]. This shape-based clustering removes jet-like or non-gradient-flow profiles, which are known to violate MOST assumptions [85-87], and retains only gradient-wind-type profiles for further analysis. As shown in Fig. 12, the SOM identifies two representative patterns: a monotonic, power-law-like profile (Pattern 1) and an S-shaped profile influenced by terrain-modified shear (Pattern 2).

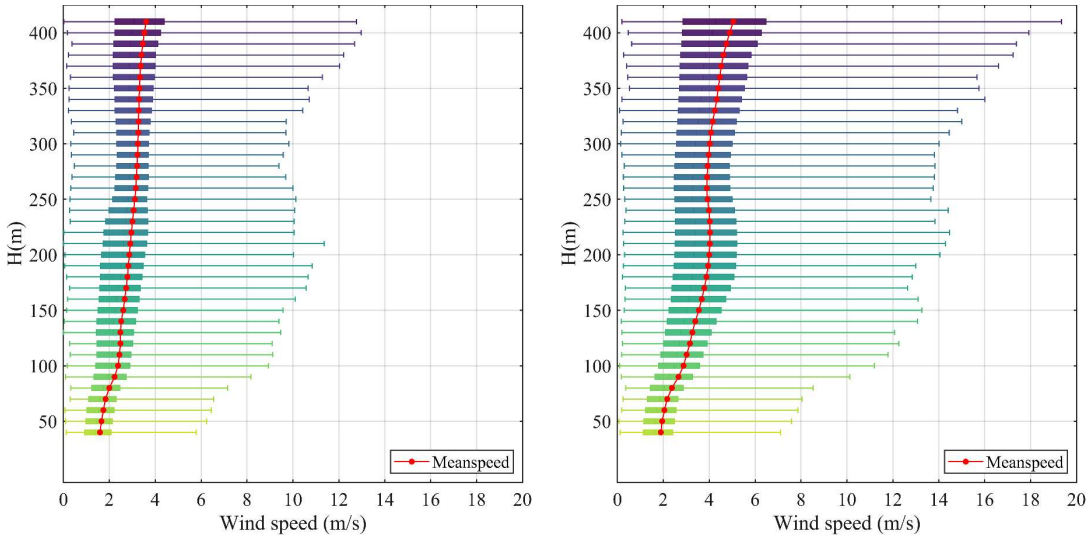

(a) Pattern 1 (P1): monotonic, power-law-like profiles

(b) Pattern 2 (P2): S-shaped profiles influenced by terrain-modified shear

Fig. 12 Wind-profile patterns identified by SOM clustering

The two identified patterns correspond to distinct physical regimes in the deep-canyon environment. Pattern 1 exhibits a smooth, nearly linear increase with height, resembling the classical power-law wind profile and indicating that the vertical shear is governed primarily by large-scale gradient flow. Pattern 2 displays an S-shaped structure associated with ridge-induced flow

modification and thermally driven circulations commonly observed in mountainous terrain. At this site, aggregation effects confine the wind direction to a nearly uniform orientation between 50 and 250 m, with veering occurring only above this layer [3]. Because this veering height exceeds the typical MOST reconstruction range of approximately 100–150 m above the reference level [22-23, 88], the weak-horizontal-gradient and homogeneity assumptions can be considered valid for both patterns within the target height range. These two flow regimes, therefore, form the basis for deriving separate stability functions and applying the proposed correction model under complex-terrain conditions.

4.1 Challenges to traditional stability-corrected wind profile models

Before introducing a new correction model based on atmospheric stability, it is necessary to clarify the rationale for its development and to define its applicable conditions. This section discusses two issues that reveal the challenges faced by existing wind profile correction models.

4.1.1 Calculation of universal function

As noted in Section 1, wind events driven by thermally driven circulations often exhibit the co-occurrence of unstable atmospheric conditions and intense winds, and they frequently display wind–temperature consistency. The following presents a representative case from a mountainous site to further illustrate this issue, with the calculations performed using Eq.(25) to Eq.(26) and the results shown in Fig. 13:

$$U(z) = \frac{u_*}{\kappa} \ln\left(\frac{z}{z_0}\right) \tag{25}$$

$$\Phi_m = \frac{\kappa}{u_*}\frac{dU}{dz} = \frac{\kappa}{u_*}\frac{U_2 - U_1}{\overline{z} \times \ln\dfrac{z_2}{z_1}} \tag{26}$$

where Φ_m denotes the wind profile universal function, and U_2 and U_1 represent the measured mean wind speeds at heights z_2 and z_2, respectively, which in this study correspond to 50 m and 10 m above ground. The numerator of the expression reflects the observed wind speed difference between two levels, while the denominator represents the theoretical wind speed difference derived from the gradient wind model. A ratio greater than 1 indicates a steeper observed wind profile gradient than the theoretical one (Eq.(25)); conversely, a value less than 1 implies a weaker gradient.

Fig. 13 shows the scatter plot of Obukhov length L (Eq.(4)) and the universal wind profile function Φ_m (Eq.(26)) derived from measured data in mountainous terrain using classical gradient-based formulations (Eq.(25)). The scatter points are computed using the stationary decomposition to demonstrate the prevalent co-occurrence of intense winds and unstable stratification.

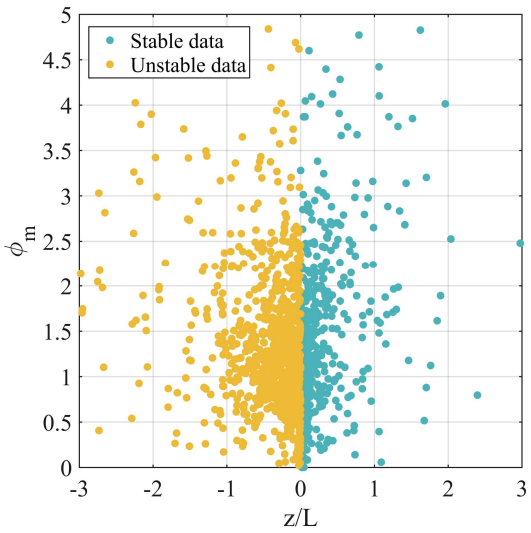

Fig. 13 Distribution of atmospheric stability and the wind profile universal function

According to traditional theory, this ratio should be less than 1 under unstable atmospheric conditions and greater than 1 under stable conditions. However, as shown in Fig. 13, a substantial number of cases exhibit values greater than 1 even under unstable conditions. This discrepancy highlights the need to redefine the atmospheric stability correction function, providing new perspectives for both wind engineering applications and the extension of Monin–Obukhov Similarity Theory to complex terrain.

4.1.2 Influence of time–frequency decomposition methods

To address the pervasive nonstationarity of wind fields in complex mountainous terrain, time–frequency decomposition is a key approach for extracting turbulent fluctuations. Nevertheless, the chosen decomposition can influence both the formulation and performance of the proposed stability-corrected wind profile model.

To examine how different detrending approaches influence the estimation of turbulent momentum flux, the friction velocity u_* (Eq.(3)) was computed from the fluctuating wind components extracted using both the stationary fixed-window method and the nonstationary DWT-based decomposition. Because u_* is directly linked to the momentum exchange coefficient in MOST, differences in its distribution reflect the sensitivity of stability corrections to the chosen

565 decomposition method. Fig. 14 compares the resulting u_* distributions for the two wind-profile
566 patterns (P1 and P2) under stable $L>0$ and unstable $L<0$ conditions.

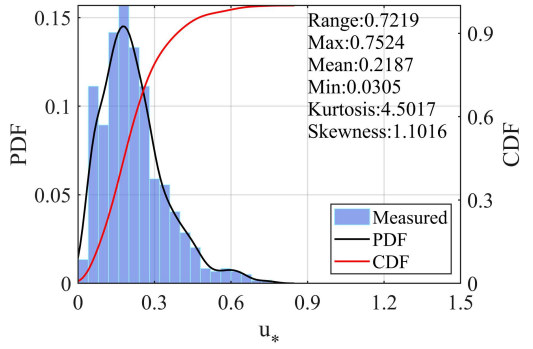

(a1) P1-Nonstationary method (Stable)

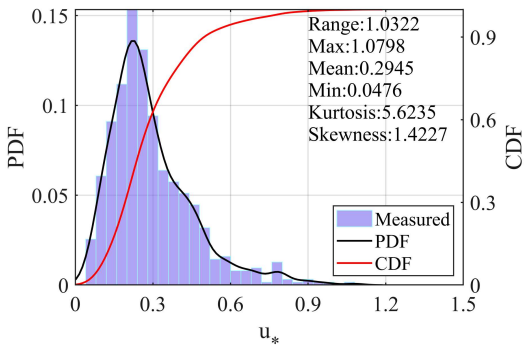

(b1) P1-Stationary method (Stable)

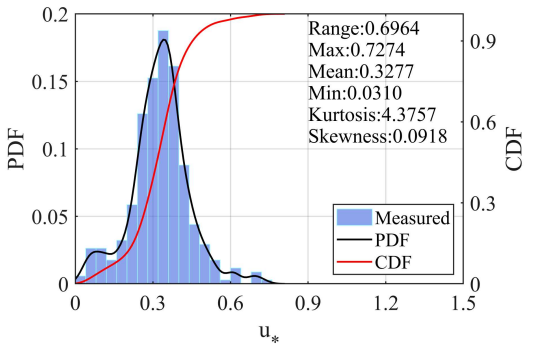

(a2) P1-Nonstationary method (Unstable)

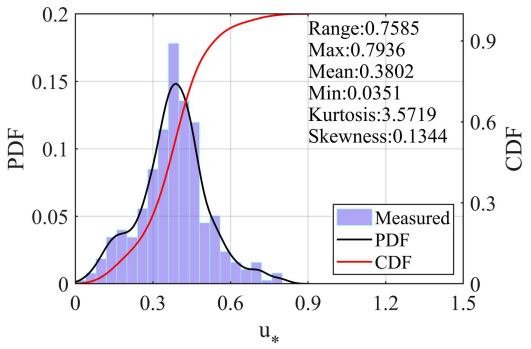

(b2) P1-Stationary method (Unstable)

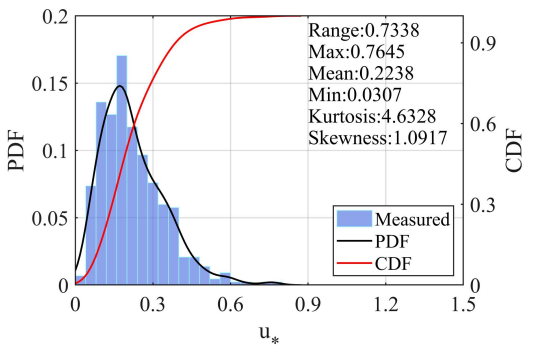

(a3) P2-Nonstationary method (Stable)

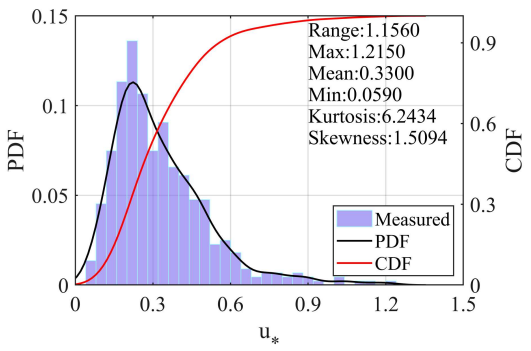

(b3) P2-Stationary method (Stable)

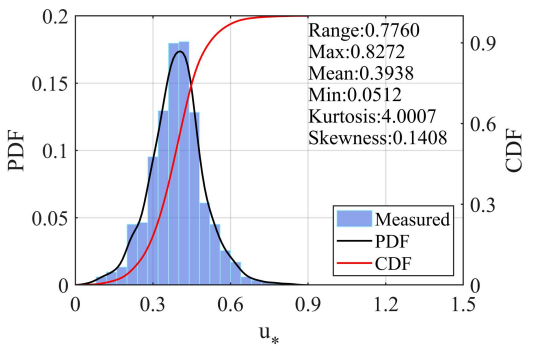

(a4) P2-Nonstationary method (Unstable)

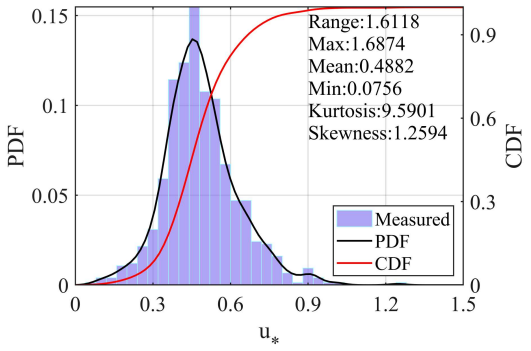

(b4) P2-Stationary method (Unstable)

Fig. 14 Distributions of friction velocity u_* obtained using stationary and nonstationary (DWT) detrending methods

As shown in Fig. 14, the friction velocity u_* computed using the DWT-based nonstationary decomposition is systematically lower than that obtained from the conventional stationary fixed-window method across both wind-profile patterns and stability regimes. This reduction reflects the more effective removal of low-frequency nonstationary motions, which reduces the covariance and therefore lowers the estimated momentum flux. In contrast, the stationary method retains portions of these large-scale motions within the fluctuation component, producing inflated u_* values and broader distributions.

The higher skewness and kurtosis observed under the stationary method further indicate that residual nonstationary disturbances amplify tail behavior and introduce terrain-induced outliers, whereas the nonstationary decomposition yields distributions closer to Gaussian turbulence. Such artifacts directly affect MOST-based scaling: because the numerator of the universal wind-profile function in Eq.(26) depends on the ratio between wind-speed differences and u_*, an inflated u_* suppresses the function value, thereby contributing to the underestimation of gradient winds noted earlier.

Table 1 compares the u_* distributions across the wind-profile patterns by conducting pairwise two-sample Kolmogorov–Smirnov (K–S) tests to assess the statistical significance of distributional differences under the different stability regimes, reporting p-values and Cliff's delta (δ) to quantify distributional differences.

Table 1 Significance testing between Stationary and Nonstationary methods

Dataset	P1-Stable	P1-Unstable	P2-Stable	P2-Unstable
p-value	<0.0001	<0.0001	<0.0001	<0.0001
Cliff's delta (δ)	-0.2976	-0.2741	-0.3768	-0.4143

Following common guidelines and previous studies [89-91], a p-value < 0.05 indicates a statistically significant difference in distributions. For Cliff's delta (δ), $|\delta| \geq 0.147$ indicates discernible differences between two distributions. Accordingly, Table 1 shows that, across the four groups, the pairwise comparisons reveal distributional differences, indicating that different methods exhibit distinct friction velocity distributions.

Given the above two issues, the traditional wind profile correction model exhibits limitations. Therefore, it is necessary to derive a new wind profile correction model based on field measurements

and tailored to the wind environment characteristics of the structure's location.

4.2 Gradient wind correction model based on Monin-Obukhov Similarity Theory

Based on the gradient wind model, by introducing the Obukhov length, the wind profile universal function that accounts for atmospheric stability is expressed in the form of Eq.(27). The universal function represents the deviation of the gradient wind from the neutral stratification within the atmospheric stability layers. When the atmosphere is in a neutral state (with a large absolute value of the Obukhov length), the universal function should approach 1, indicating that neutral stratification is unaffected by turbulent transport characteristics and reverts to the general gradient wind model. This assumption is based on MOST, which states that the ratio of wind speed and temperature universal functions should be equal to the corresponding turbulent exchange coefficient, as shown in Eq.(28).

$$\frac{\kappa z}{u_*}\frac{du}{dz} = \Phi_m\left(\frac{z}{L}\right) \tag{27}$$

$$\frac{\Phi_h}{\Phi_m} = \frac{K_h}{K_m} = \gamma \tag{28}$$

Where Φ_h is the universal function for the temperature profile, and Φ_m is the universal function for the wind speed profile, K_h is the turbulent heat exchange coefficient, K_m is the turbulent momentum exchange coefficient, and γ is the constant ratio between the turbulent exchange coefficients.

4.2.1 The empirical stability function satisfying the MOST correction framework

To quantify the influence of atmospheric stability on wind speed flow in the vertical direction and to correct the wind profile under different turbulent flux conditions, the neutral component in Eq.(27) should be removed, and an integration is performed over the vertical height. This process yields the correction function for atmospheric stability in Eq.(29) and the corresponding corrected wind profile model in Eq.(30). Therefore, the "influencing factor" of the correction function with height can be extracted, and its functional relationship with atmospheric stability can be considered separately. In this study, this factor is referred to as the stability function $\Phi_{ms}(z/L)$. Based on the requirements of the universal function, when the atmosphere is in a neutral state, the correction function should be zero. Similarly, the stability function Φ_{ms}(z/L) used for the correction function

integral should approach zero under neutral atmospheric conditions.

$$\psi_m\left(\frac{z}{L}\right)=-\int_{z_0}^{z}\frac{\Phi_{ms}\left(\frac{z}{L}\right)}{z}dz \tag{29}$$

$$U(z)=\frac{u_*}{\kappa}\left[\ln\left(\frac{z}{z_0}\right)-\psi_m\left(\frac{z}{L}\right)\right] \tag{30}$$

where $\Phi_{ms}(z/L)$ is the stability function obtained by removing the neutral component from the universal function.

Taking the classical Businger–Dyer (B-D) stability correction functions established over flat terrain in Eq.(31) to Eq.(33) as an example:

$$\frac{\kappa z}{u_*}\frac{du}{dz}=\Phi_m\left(\frac{z}{L}\right)=\begin{cases}1+4.7\frac{z}{L}(L..0)\\ \left(1-16\frac{z}{L}\right)^{-\frac{1}{4}}(L<0)\end{cases} \tag{31}$$

$$\psi_m\left(\frac{z}{L}\right)=-\int_{z_0}^{z}\frac{\Phi_{ms}\left(\frac{z}{L}\right)}{z}dz=-\int_{z_0}^{z}\frac{\Phi_m\left(\frac{z}{L}\right)-1}{z}dz \tag{32}$$

$$\psi_m=\begin{cases}-4.7\frac{z}{L}(L>0)\\ \ln\frac{1+x^2}{2}+2\ln\frac{1+x}{2}-2arctgx+\frac{\pi}{2}\left(x=\left(1-16\frac{z}{L}\right)^{\frac{1}{4}},L<0\right)\end{cases} \tag{33}$$

Its correction function Eq.(33) is derived based on the form of Eq.(32). The stability function $\Phi_{ms}(z/L)$ is derived by subtracting a value of one from the universal function, ensuring it approaches zero under neutral conditions. Its corresponding integral over height can also be understood as removing the neutral component represented by the $1/z$ gradient integral, indicating that this part is considered unaffected by turbulent transport in the atmosphere.

Atmospheric stability varies across different terrains and thermal conditions, making it challenging to establish a universal function that strictly satisfies the similarity criterion shown in Eq.(28). Typically, empirical fitting is required based on observed data characteristics to accommodate different turbulent transport features [26]. Therefore, following the correction function derivation process from Eq.(27) to Eq.(30), constructing an empirical stability function

that meets the integral requirements and effectively captures deviations from neutral atmospheric conditions based on locally measured data is a reasonable approach. Directly integrating the empirical stability function avoids the complex derivation of the universal function and the determination of neutral conditions during stability function construction, making it more suitable for engineering applications in complex terrain. The process should adhere to the MOST correction framework:

(1) The stability function should be constructed based on a universal function that satisfies the similarity criterion, ensuring compliance with the requirements of Eq.(27) and Eq.(28).

(2) The stability function should effectively capture deviations from neutral atmospheric stratification, meaning its value should approach zero under neutral conditions. Additionally, it should possess the capability to adjust wind speed across different heights smoothly, ensuring integrability in the vertical direction, in accordance with the requirements of Eq.(29).

(3) The integral of the stability function over vertical height, which forms the correction function, should also reflect deviations from neutral atmospheric stratification. That is, the integrated correction function should approach zero under neutral stratification conditions, ensuring compliance with the requirements of Eq.(30).

It is important to note that this integration process assumes that the turbulent flux and wind direction remain nearly constant with height, indicating that their variations with height are considered negligible [83].

4.2.2 Determination of the empirical stability function and universal function

Under stable atmospheric conditions, the universal function that satisfies the similarity criterion is typically parameterized in a "log-linear" form in vertically stratified flows, whereas under special circumstances, a height-independent ("z-less") form may emerge [81]. Then, the stable stability function satisfies the requirements outlined in process (1) for the stability function.

$$\begin{cases} \Phi_m = \dfrac{\kappa z}{u_*}\dfrac{du}{dz} = 1 + \dfrac{\beta z}{L} \\ \Phi_{m(z-less)} = \dfrac{\kappa}{u_*}\dfrac{du}{dz} = \dfrac{\beta}{L} \end{cases} \tag{34}$$

To account for complex influences on buoyancy and heat flux, such as cases where heat flux exchange is not entirely near-surface, a special transformation can be introduced that incorporates height-independent heat flux density and vertical gradients [92]. Then, the stable stability function can satisfy the requirements outlined in process (2) for the stability function.

$$\Phi_{ms} = \frac{\kappa}{u_*}\frac{du}{dz} = c\frac{z}{L}(L \geq 0) \tag{35}$$

Under unstable atmospheric conditions, the universal function is given in Eq.(36) . The derivation, based on the Richardson number and the Businger–Dyer (B–D) relationships [93], is provided in the appendix (A3. Derivation of the Universal Function for Unstable Stratification). Then, the unstable stability function satisfies the requirements outlined in process (1) for the stability function.

$$\Phi_m = a(1-b\frac{z}{L})^{-\frac{1}{4}}(b > 0) \tag{36}$$

In Eq.(36), the universal function approaches a under neutral conditions. Therefore, the function can be rewritten in the form of Eq.(37). Then, the unstable stability function satisfies the requirements outlined in process (2) for the stability function.

$$\Phi_{ms} = a(1-b\zeta)^{-\frac{1}{4}} - a \tag{37}$$

(1) *Construction of the empirical stability function*

Based on Eq.(35) and Eq.(37), the new stability function can be expressed as:

$$\Phi_{ms}\left(\frac{z}{L}\right) = \begin{cases} c\dfrac{z}{L} & (L..0) \\ a\left(1-b\dfrac{z}{L}\right)^{-\frac{1}{4}} - a & (L < 0) \end{cases} \tag{38}$$

Where z=50 m, L is the Obukhov length, and a, b, c are fitting coefficients.

(2) *Derivation of the correction function*

Referring to the transformation of the corresponding stability function in Eq.(32) based on Eq.(31), the unstable stability function in Eq.(38) can be rewritten in the form of Eq.(33) after substituting it into Eq.(29). If the integration process of the correction function represented by Eq.(33) is regarded as $\psi'_m(z/L)$, the unstable correction function with updated coefficients can be transformed into the form of Eq.(39), the calculation steps can be simplified, and the new correction function can be expressed in the form of $a*\psi'_m(z/L)$.

$$\psi_m\left(\frac{z}{L}\right)=-\int_{z_0}^{z}\frac{a\Phi_m\left(\frac{z}{L}\right)-a}{z}dz=a\cdot\psi'_m\left(\frac{z}{L}\right) \tag{39}$$

Referring to the treatment of the stable correction function in Eq.(33), removing the constant term related to z_0, the new correction function can be derived as:

$$\psi_m\left(\frac{z}{L}\right)=\begin{cases}-\frac{c}{L}\cdot \mathrm{z} \quad (L\geq 0)\\ a(\ln\frac{1+x^2}{2}+2\ln\frac{1+x}{2}-2arctgx+\frac{\pi}{2}) \quad (x=\left(1-b\frac{z}{L}\right)^{\frac{1}{4}},L<0)\end{cases} \tag{40}$$

The correction function satisfies the requirements outlined in the process (3), meaning its value approaches zero under neutral conditions. In the final correction function, a denotes the unstable-atmosphere (upward heat flux) correction coefficient for complex terrain. A positive a indicates that the net atmospheric effect inferred from the single-site measurements, including the combined influence of canyon topography and surface roughness, suppresses the gradient mean flow. A negative a indicates an enhancement of the mean flow. The absolute value of $|a|$ quantifies the strength of this suppression/enhancement on the gradient wind. Parameter b is a shape parameter for the unstable-atmosphere correction, introduced to improve the flexibility of the functional form; it is constrained to be positive. Parameter c denotes the stable-atmosphere (downward heat flux) correction coefficient for complex terrain. Because the heat-flux direction is reversed, the sign of c is interpreted oppositely to a with respect to its effect on the mean flow, and $|c|$ likewise measures the magnitude of that effect.

4.3 Correction result

The applicability of the MOST decreases when the wind speed is too low, and the Obukhov length exhibits strong randomness [94]. Therefore, measured wind profiles with a maximum wind speed greater than 5.5 m/s were selected for stability function calculation and corresponding coefficient fitting. The corresponding values of the universal function are obtained based on the mean wind speed at 50 m and 10 m meteorological towers, calculated using Eq.(26). Fit results for each wind-profile pattern under the stationary and nonstationary decompositions are shown in Fig. 15. The red-shaded region denotes the 95% confidence interval (CI) of the fitted curve.

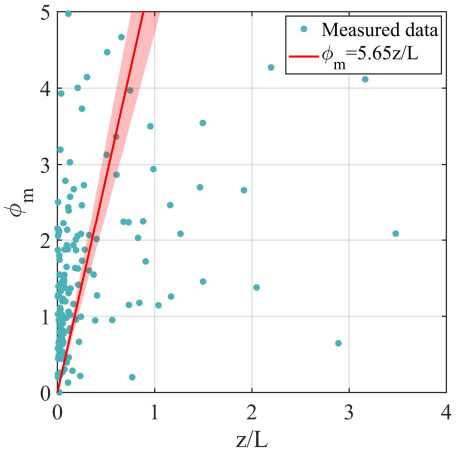

(a1) P1-Nonstationary method (Stable)

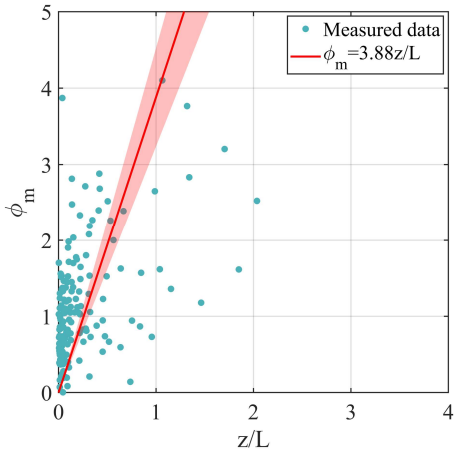

(b1) P1-Stationary method (Stable)

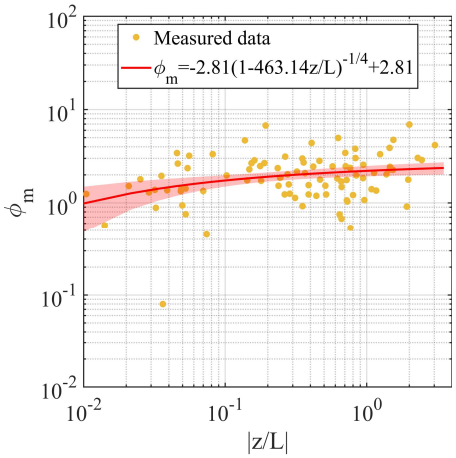

(a2) P1-Nonstationary method (Unstable)

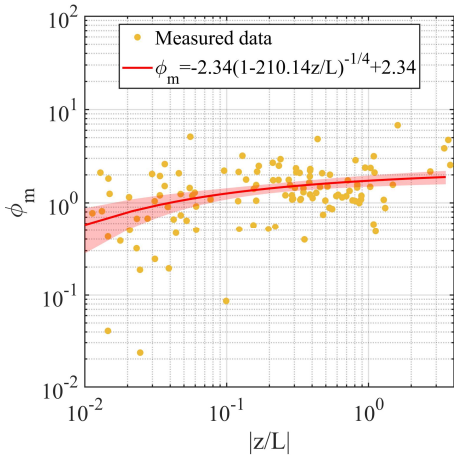

(b2) P1-Stationary method (Unstable)

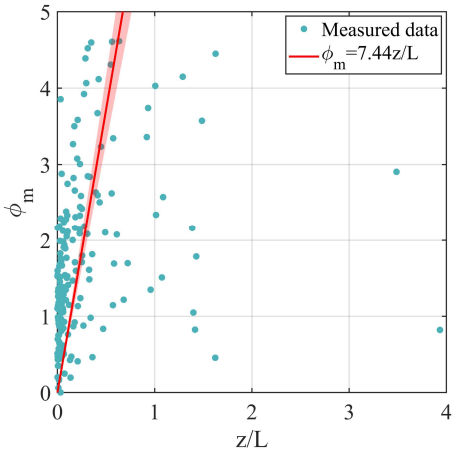

(a3) P2-Nonstationary method (Stable)

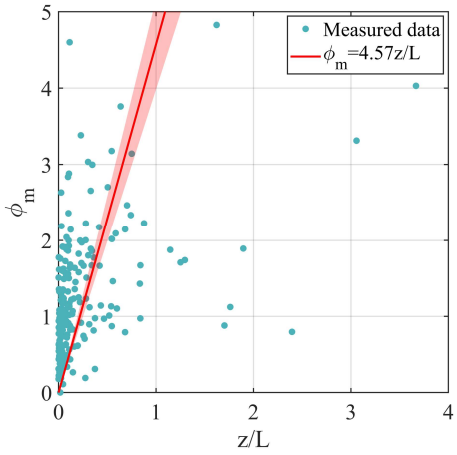

(b3) P2-Stationary method (Stable)

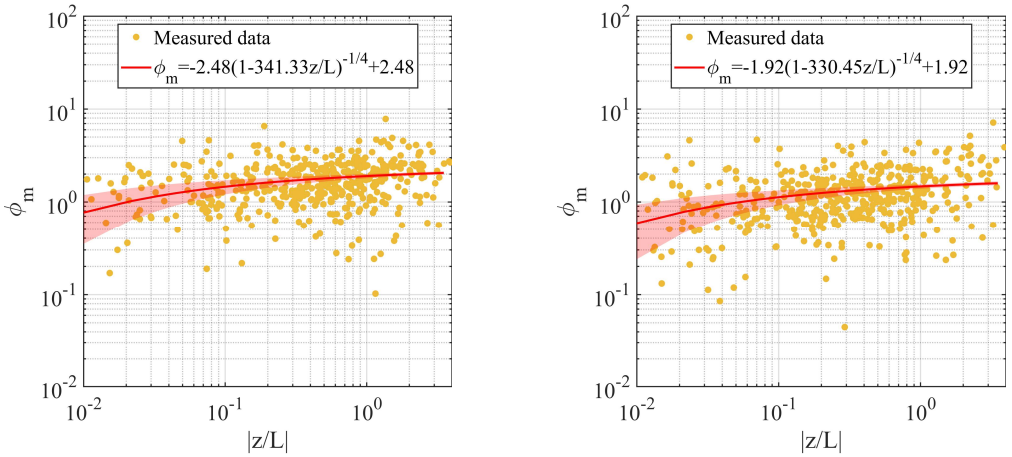

(a4) P2-Nonstationary method (Unstable) (b4) P2-Stationary method (Unstable)

Fig. 15 Stability function representation for each wind profile pattern

As shown in Fig. 15, the new atmospheric stability correction model demonstrates good agreement between the fitted curves and the measured samples. In unstable conditions, a substantial fraction of the observations yield stability functions exceeding 1, consistent with the findings reported in Section 4.1.1. Moreover, comparison of Fig. 14a and 14b shows that a larger friction velocity leads to smaller fitted values, in agreement with the discussion in Section 4.1.2. For Pattern 1 wind profiles, stable conditions dominate with relatively few unstable samples, while Pattern 2 is primarily characterized by unstable conditions. These results indicate that atmospheric stability directly influences the shape of wind profiles.

Based on the gradient wind model (Eq.(25)), the energy loss and momentum transfer at a given height z_r can be derived. These effects are typically represented by the drag coefficient C_d (Eq.(41)).

$$C_d = \frac{\tau_0}{\rho U^2} = \frac{u_*^2}{U^2} \tag{41}$$

Moreover, at the reference height z_r, Eq.(41) can be transformed into the form of Eq.(42):

$$u_* = U_r C_{dr}^{1/2} \tag{42}$$

By substituting the new correction function into Eq.(30), the gradient wind profile can be corrected using the MOST method to account for the atmospheric stability near the surface (Eq.(43)). This formulation produces an improved wind speed profile model that incorporates the effects of atmospheric stratification stability and mountainous terrain influences.

$$U = U_{z_r} - \frac{U_{z_r} C_{dz_r}^{1/2}}{\kappa} \ln\left(\frac{z_r}{z}\right) - \frac{U_{z_r} C_{dz_r}^{1/2}}{\kappa}\left[\psi_m\left(\frac{z}{L}\right) - \psi_m\left(\frac{z_r}{L}\right)\right] \tag{43}$$

Taking the 50 m height as the reference height, the corrected wind profiles for each pattern are plotted in Fig. 16. The shaded regions around the fitted curves denote the corresponding 95% confidence intervals. Additionally, the atmospheric stability profiles calculated using the empirical B-D and Holtslag [95] correction function from Eq.(33) and Eq.(44) are also included for comparison.

$$\psi_m = \begin{cases} -\frac{z}{L} - \frac{2}{3}\left(\frac{z}{L} - \frac{5}{0.35}\right)\exp\{-0.35\frac{z}{L}\} - \frac{\frac{2}{3}\times 5}{0.35} & (L > 0) \\ 1.5\ln\left(\frac{1+y+y^2}{3}\right) - \sqrt{3}\arctan\left(\frac{2y+1}{\sqrt{3}}\right) + \frac{\pi}{\sqrt{3}} & (y = \left(1 - 13\frac{z}{L}\right)^{\frac{1}{3}}, L < 0) \end{cases} \tag{44}$$

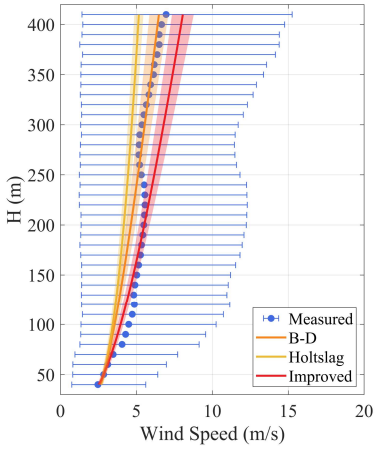

(a1) P1-Nonstationary method (all)

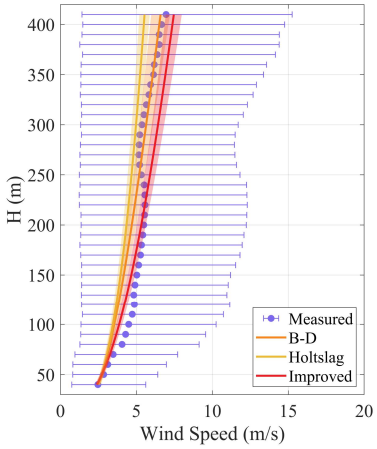

(b1) P1-Stationary method (all)

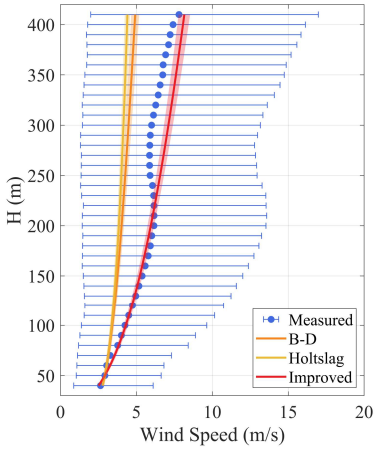

(a2) P2-Nonstationary method (all)

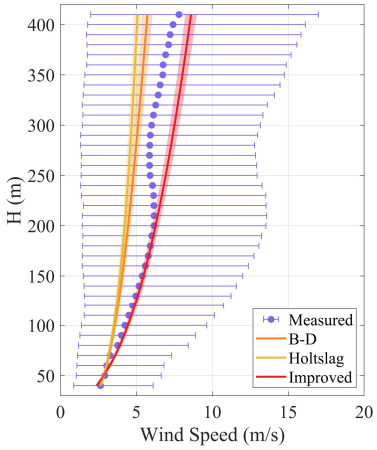

(b2) P2-Stationary method (all)

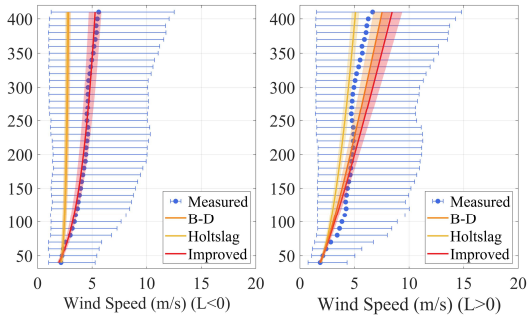

(a3) P1-Nonstationary method (classification)

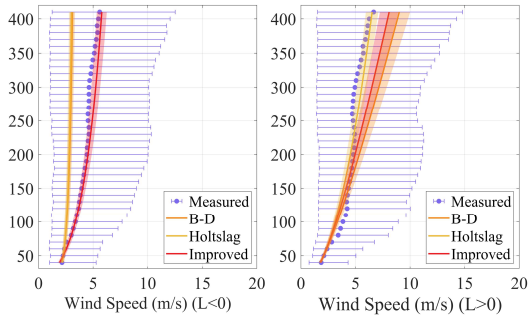

(b3) P2-Stationary method (classification)

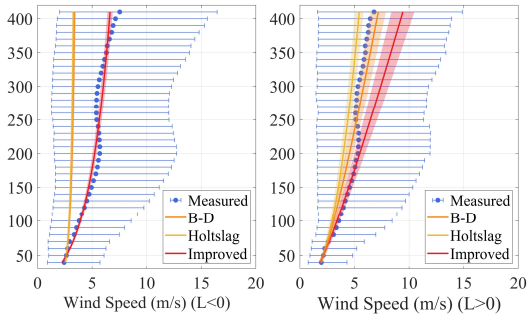

(a4) P1-Nonstationary method (classification)

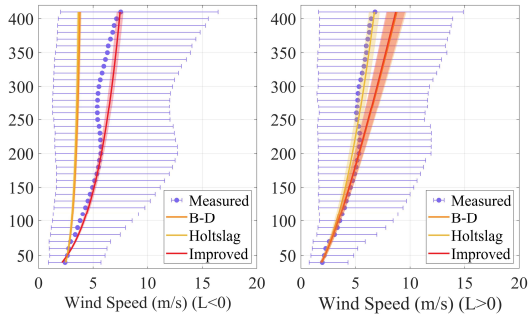

(b4) P2-Stationary method (classification)

Fig. 16 Mountainous wind profile correction model considering atmospheric stability

As shown in Fig. 16, the atmospheric stability model derived using the empirical stability function underestimates the wind speed in mountainous wind profiles. Previous studies have shown that the MOST effectively corrects wind profiles within approximately 100 to 150 m above the reference height [23, 88]. The correction functions derived for Pattern 1 and Pattern 2 show better correction capability, effectively correcting wind profiles up to approximately 230 m above ground level, which is the height at which deviations in angle of attack and wind direction occur [3]. Detailed fitting accuracies for the different models are provided in Appendix Table A1 and Table A2. Regardless of whether the stationary or nonstationary decomposition is used, the improved correction model attains higher fitting accuracy. Further examination by stability class shows that under unstable conditions, the improved method is consistently superior. This is attributable to the co-occurrence of unstable stratification and thermally driven intense winds in complex mountainous terrain, a regime for which classical formulations for unstable conditions are not well suited. These correction results suggest that once an appropriate correction function is established, MOST remains applicable in complex mountainous terrain, allowing wind profiles to be adjusted based on near-surface atmospheric stability.

4.4 Application method and case study of the correction model

The MOST method has been demonstrated to be an effective approach for deriving turbulence characteristics based on wind profile data. Therefore, it is necessary to establish a wind profile model related to the gradient wind profile shape (Eq.(45)) to facilitate further applications in wind engineering research.

$$u(z)=\frac{U(z)}{U(z_r)}=\frac{\left[\log\left(\frac{z}{z_0}\right)-\psi\left(\frac{z}{L}\right)\right]}{\left[\log\left(\frac{z_r}{z_0}\right)-\psi\left(\frac{z_r}{L}\right)\right]} \tag{45}$$

Eq.(45) yields the normalized wind-profile shape for different stability regimes, defined as $U(z)/U(z_r)$, where z_r is the reference height, and z_0 is the surface roughness length. Eq.(45) explicitly incorporates the correction function and z_0, it establishes a gradient wind-profile correction model that accounts for atmospheric stability. In practical engineering applications, wind-profile modelling requires only the mean wind speed specified at a near-surface reference height z_r. To assess how different profile patterns deviate from the ideal gradient-wind ($\log(z/z_0)/\log(z_r/z_0)$) reference under the action of the correction function, we first invert z_0 from the mast observations and then compile statistics separately for stable (L>0) and unstable (L<0) conditions (Fig. 17).

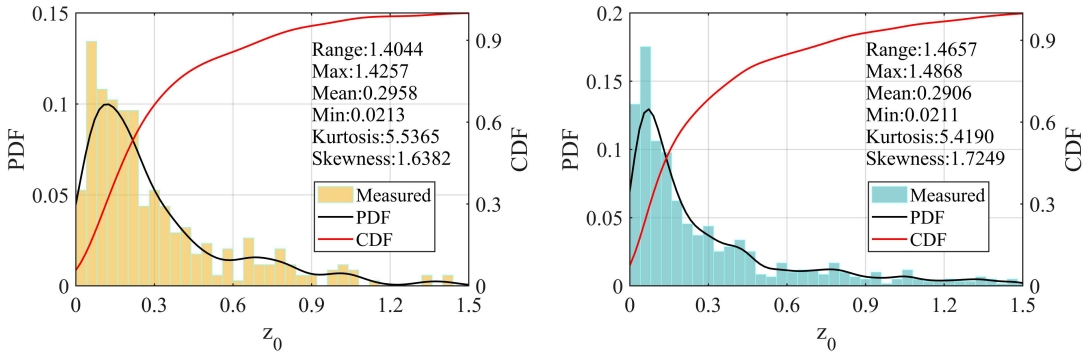

(a1) P1-Unstable

(b1) P1-Stable

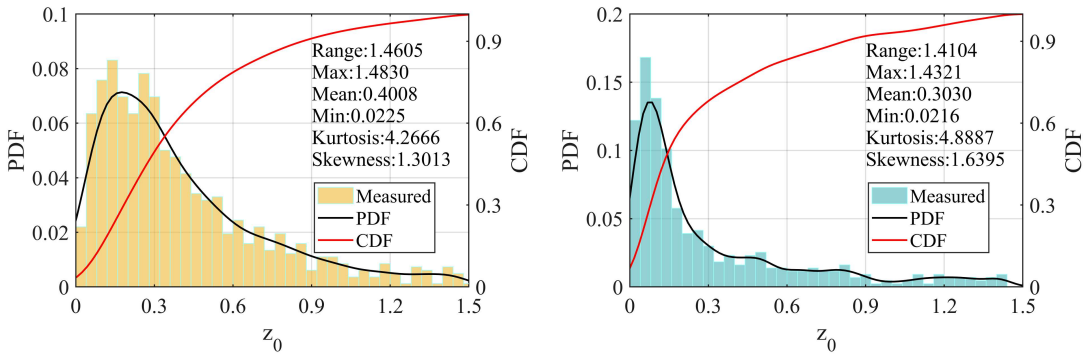

(a2) P2-Unstable (b2) P2-Stable

Fig. 17 Distribution of surface roughness z_0

Using the mean z_0 for each pattern under stable and unstable conditions from Fig. 17, we adopt a reference height z_r=10 m to better display the normalized profile shape. Substituting these values into Eq.(45) yields the wind-profile curves for each stability class, as shown in Fig. 18.

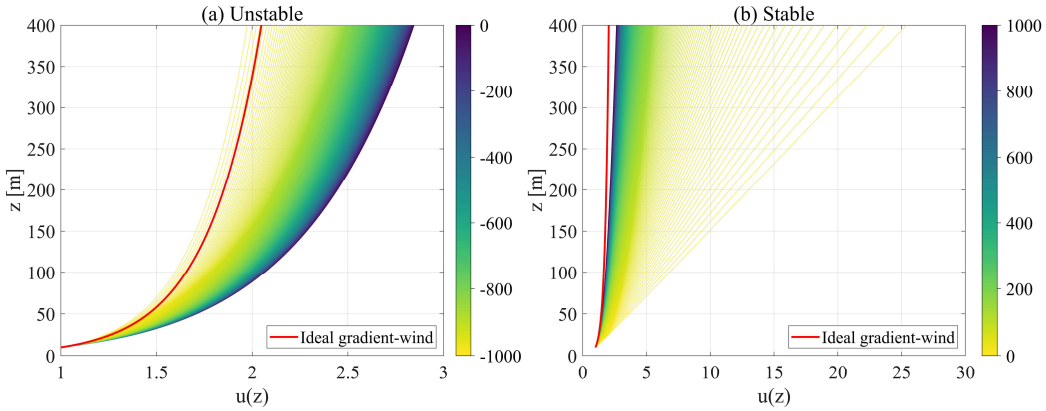

(a) Pattern 1 (Unstable z_0=0.2958, Stable z_0=0.2906)

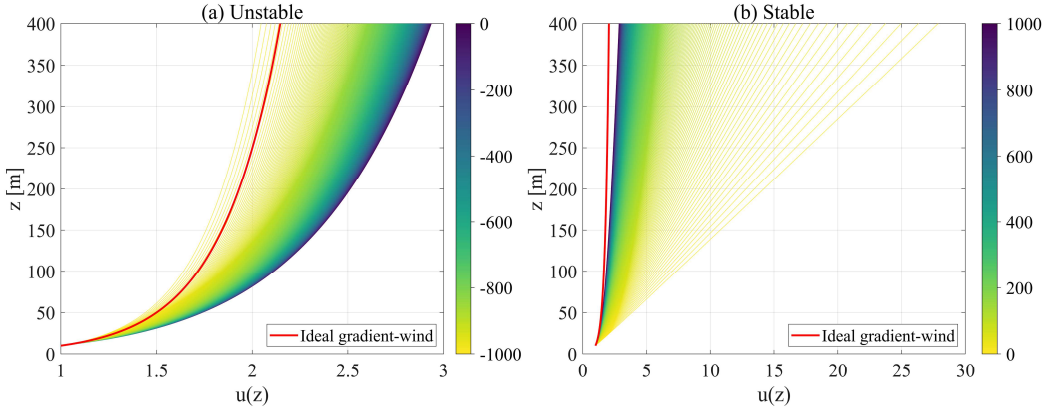

(b) Pattern 2 (Unstable z_0=0.4008, Stable z_0=0.3030)

Fig. 18 Non-dimensional logarithmic wind profile

In Fig. 18, the red line denotes the ideal gradient-wind $\log(z/z_0)/\log(z_r/z_0)$, which highlights departures from the ideal state induced by the correction function. For both patterns, within the unstable range (L > -990), the normalized profiles lie above the gradient-wind line, indicating an enhancement relative to the gradient flow. This behavior is consistent with the wind-profile correction results and supports the reliability of the proposed model.

To examine how surface characteristics influence the stability-based correction of wind profiles, we computed normalized profiles by setting z_0=0.5, 1, and 2 m (Fig. 19).

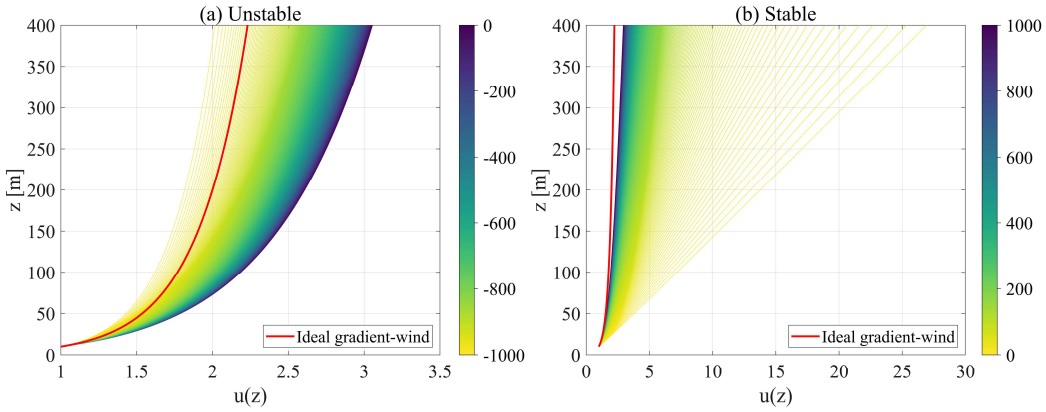

(a1) Pattern 1 (z_o=0.5)

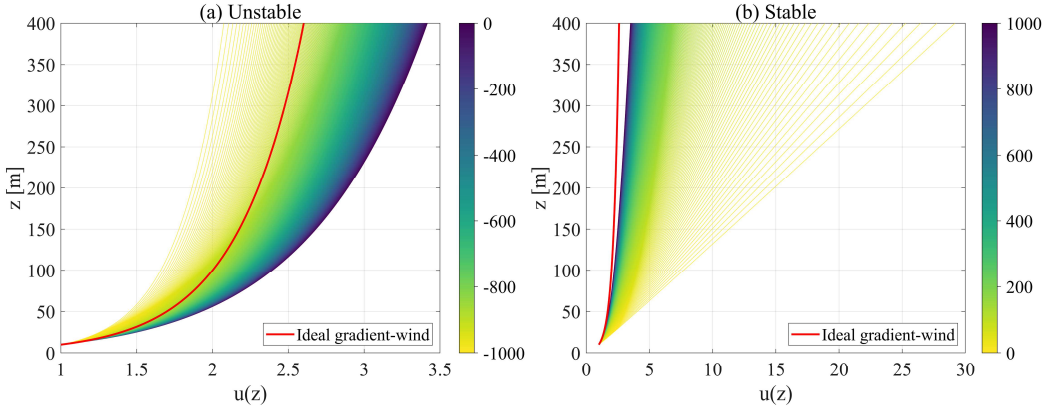

(a2) Pattern 1 (z_o=1)

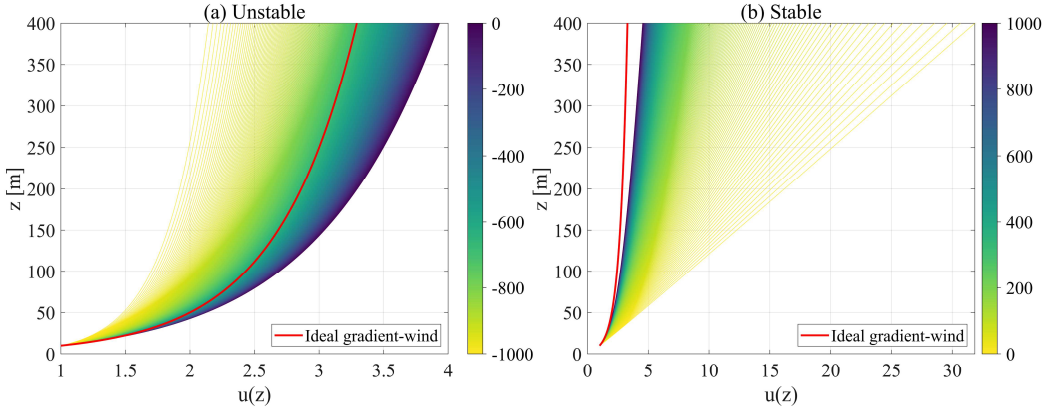

(a3) Pattern 1 (z_o=2)

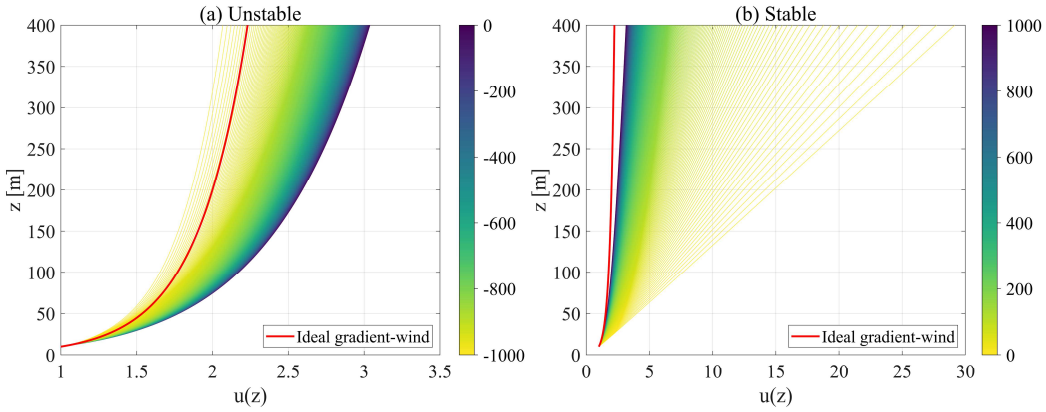

(b1) Pattern 2 (z_0=0.5)

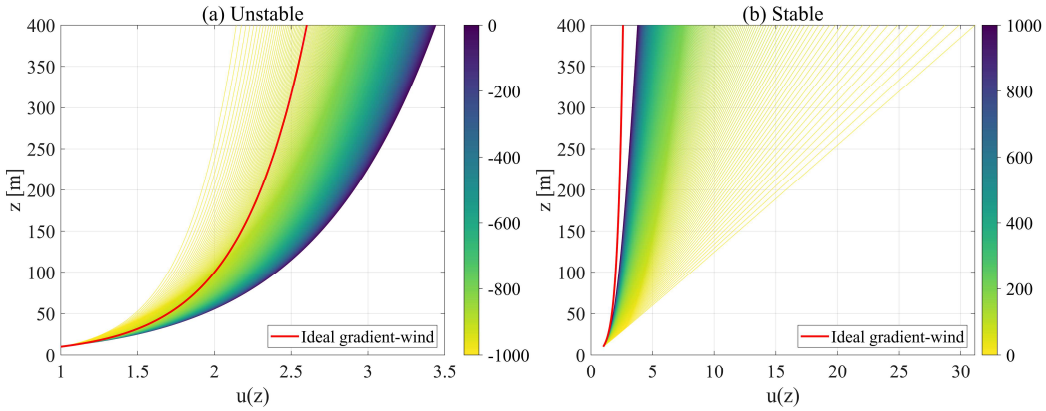

(b2) Pattern 2 (z_0=1)

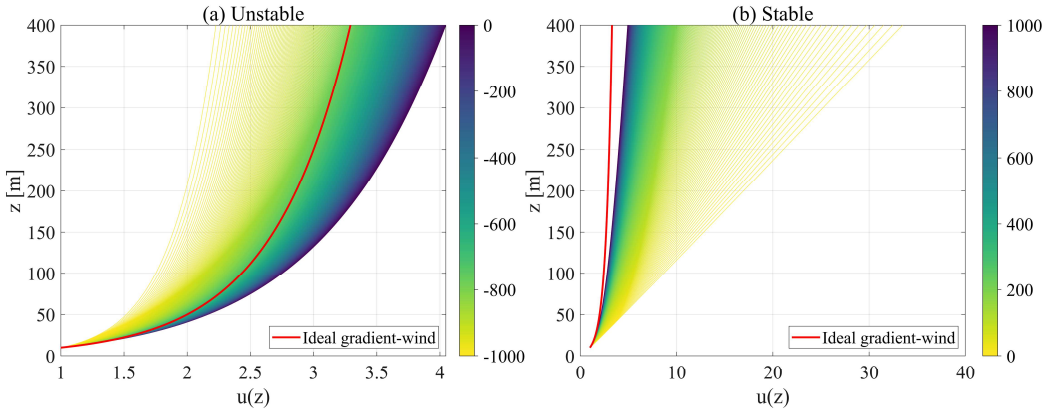

(b3) Pattern 2 (z_0=2)

Fig. 19 Non-dimensional logarithmic wind profile with different z_0

As demonstrated in Fig. 19, increasing z_0 leads to higher normalized wind speeds under both stable and unstable conditions, and the departure of the unstable profile from the ideal gradient-wind reference occurs at progressively more negative stability (L) values: for z_0=0.5 m the profile shows enhancement relative to gradient-wind for L>−990, for z_0=1 m near L≈−900; and for z_0=2 m near L≈−800. This feature indicates that application of the model requires rigorous verification of

765 the terrain-specific roughness length z_0 to avoid potential bias.

766 **5 Conclusions**

767 Based on field measurement data, this study compared stationary and nonstationary models to
768 determine appropriate methods for extracting turbulent fluctuations and corresponding heat fluxes,
769 providing a valuable reference for turbulence decomposition and atmospheric stability calculation
770 in complex mountainous terrain. A wind profile correction model consistent with the Monin–
771 Obukhov similarity theory (MOST) framework was developed, linking complex terrain turbulence
772 characteristics with vertical wind profile structures. The model was validated using field
773 measurements. The main conclusions are as follows:

774 1. Under strong convective conditions induced by temperature gradients and when extracting
775 turbulent fluctuations using time-frequency methods, the applicability of the classical
776 MOST-based wind profile correction model is notably reduced.
777 2. The stationary model is not well-suited for nonstationary wind fields in complex terrain.
778 In the nonstationary model, the discrete wavelet transform outperforms the moving
779 average method in both signal correlation decomposition and turbulent kinetic energy
780 distribution.
781 3. Cospectral analysis effectively identifies the coupled transport of turbulent wind and heat
782 extracted via nonstationary decomposition methods and enables a reasonable selection of
783 the optimal decomposition level for the discrete wavelet transform.
784 4. An atmospheric stability-corrected wind profile model was derived and validated; it
785 constructs an empirical stability function within the MOST framework and captures the
786 terrain-specific behavior of the universal functions, ensuring applicability to nonstationary
787 wind fields in complex mountainous terrain.
788 5. A case study demonstrates the wind engineering application of the proposed correction
789 model, in which an established correction relationship between turbulent components and
790 wind profiles enables reconstruction of the vertical wind profile from near-surface mean
791 wind speeds, with effective correction heights of 150–200 m above the reference level.
792 6. Limitations and scope of applicability: The method is intended for complex terrain where
793 pronounced thermal signatures and thermally driven intense winds co-occur under
794 unstable stratification, with profiles screened to satisfy the weak horizontal-gradient

assumption (gradient-wind-type profiles without significant veering within the correction-height range). A full flux budget/closure analysis was not feasible given the measurement layout; the correction framework was evaluated at a single site, and thus its external validity/generalizability remains to be established.

Data availability statement:

The data that support the findings of this study are available from the corresponding author upon reasonable request.

Acknowledgment

The work conducted for this paper was supported by the National Natural Science Foundation of China (No.52278533) and Natural Science Foundation of Sichuan Province (Nos. 2023NSFSC1961 and 2022NSFSC0004).

APPENDIX

A1.Three independent time periods.

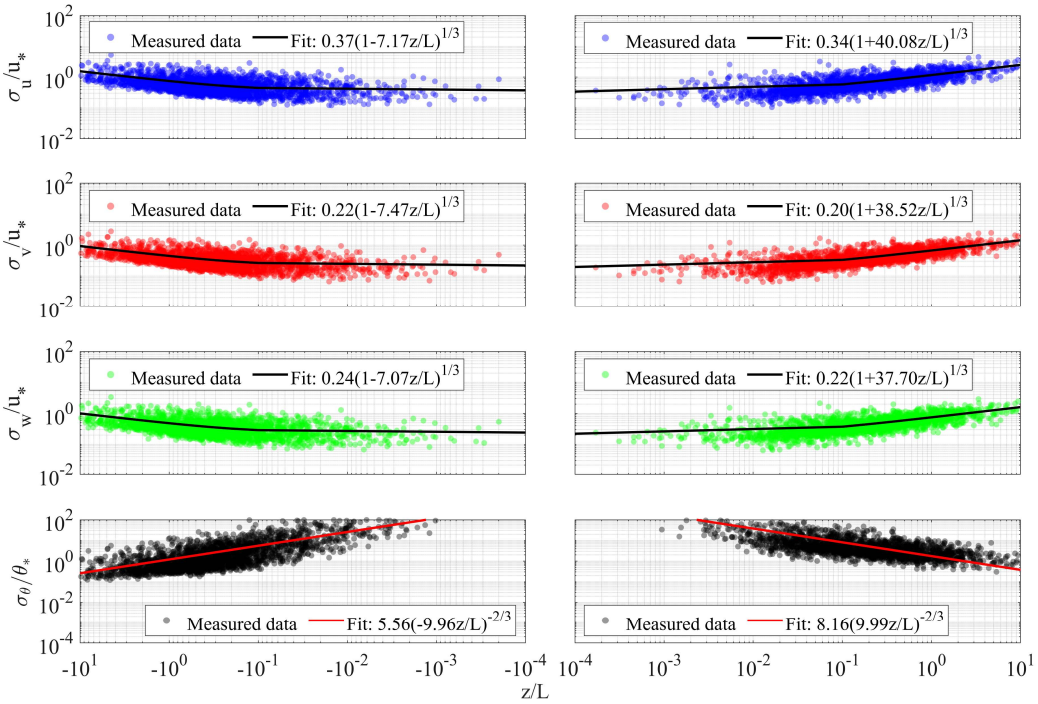

(a) Spring (April–May 2017)

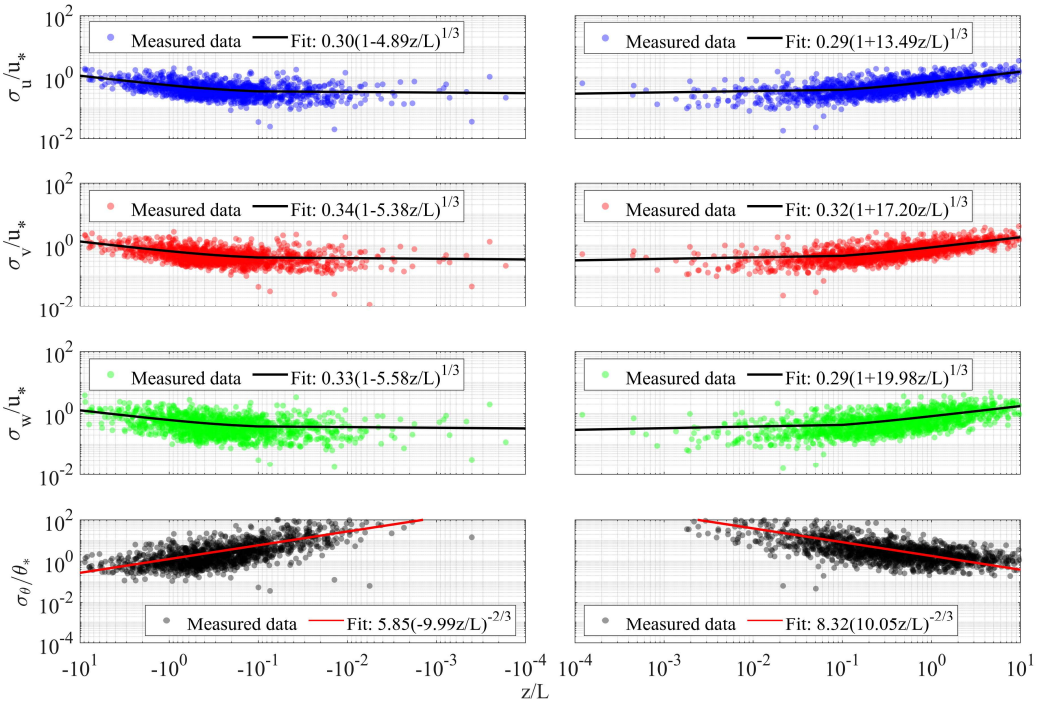

(b) Summer (July–August 2017)

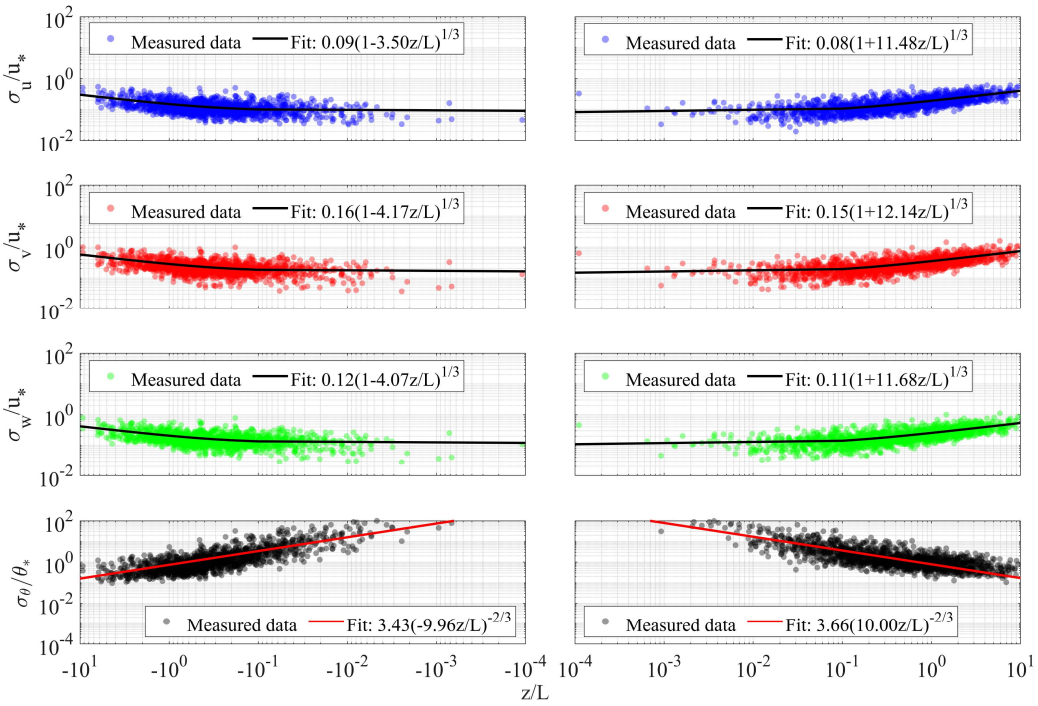

(c) Autumn (October–November 2017)

Fig. A1 Three independent time periods

A2.Cumulative cospectrum of three typical time series

Fig. A2 shows the cumulative cospectral integrals for the three representative event time series. Pattern 3 corresponds to the jet-like wind profile that was removed in bulk in this study; it is shown here solely as a representative wind type to illustrate the general applicability of the cospectral method and is not included in the wind-profile correction calculations. For Event 1 and Event 3, the selected time series are dominated by stable stratification (downward sensible heat flux), so the cospectral values are negative. To enable plotting on logarithmic axes, the spectra are displayed with the sign reversed.

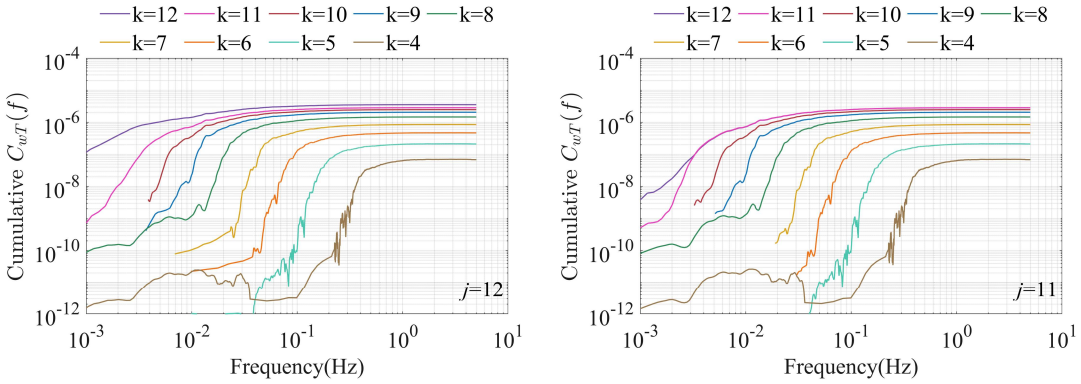

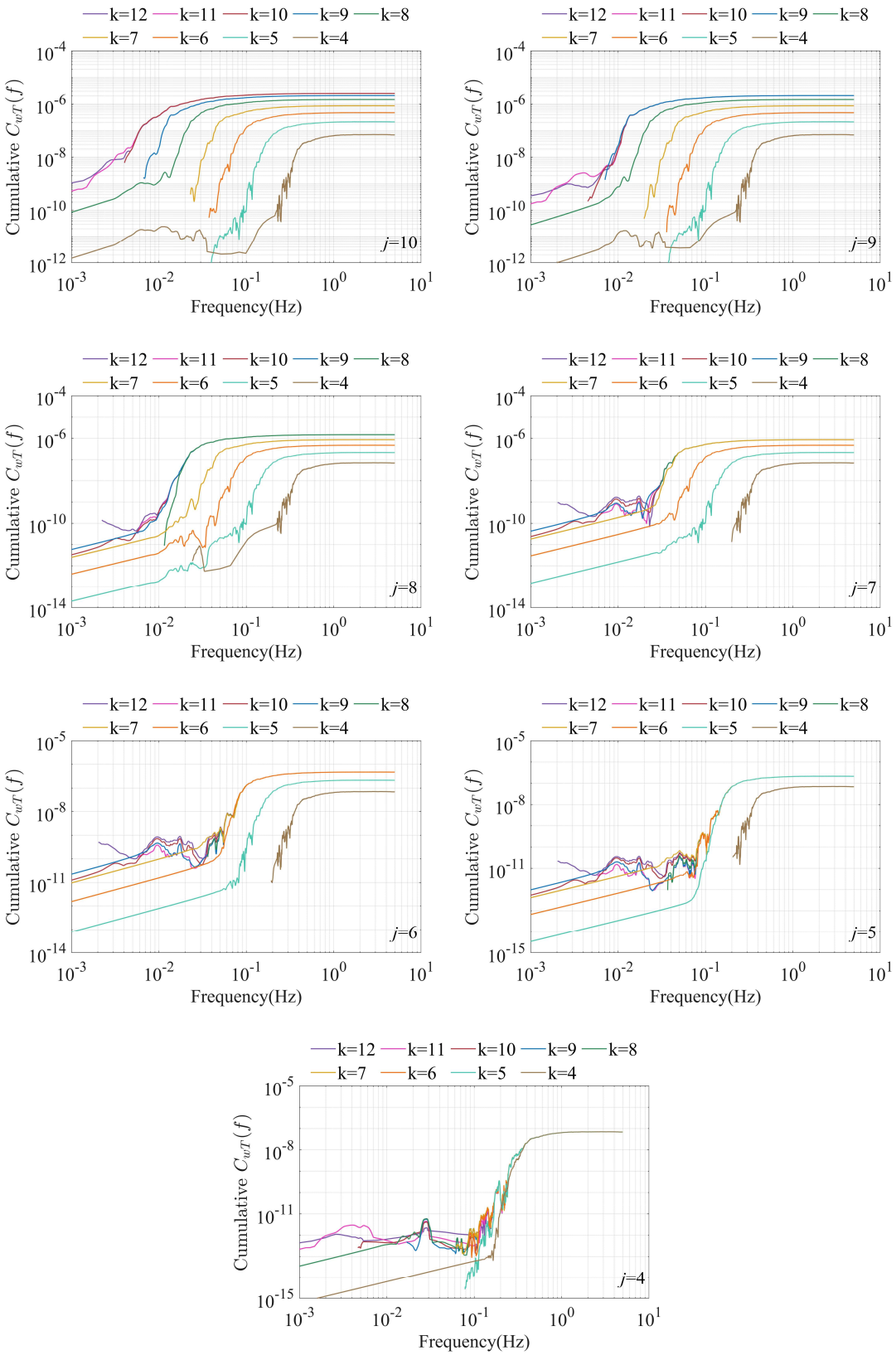

(a) Event 1: June 6, 2017, 20:00 to 22:00, Pattern 1 wind profile (Neutral)

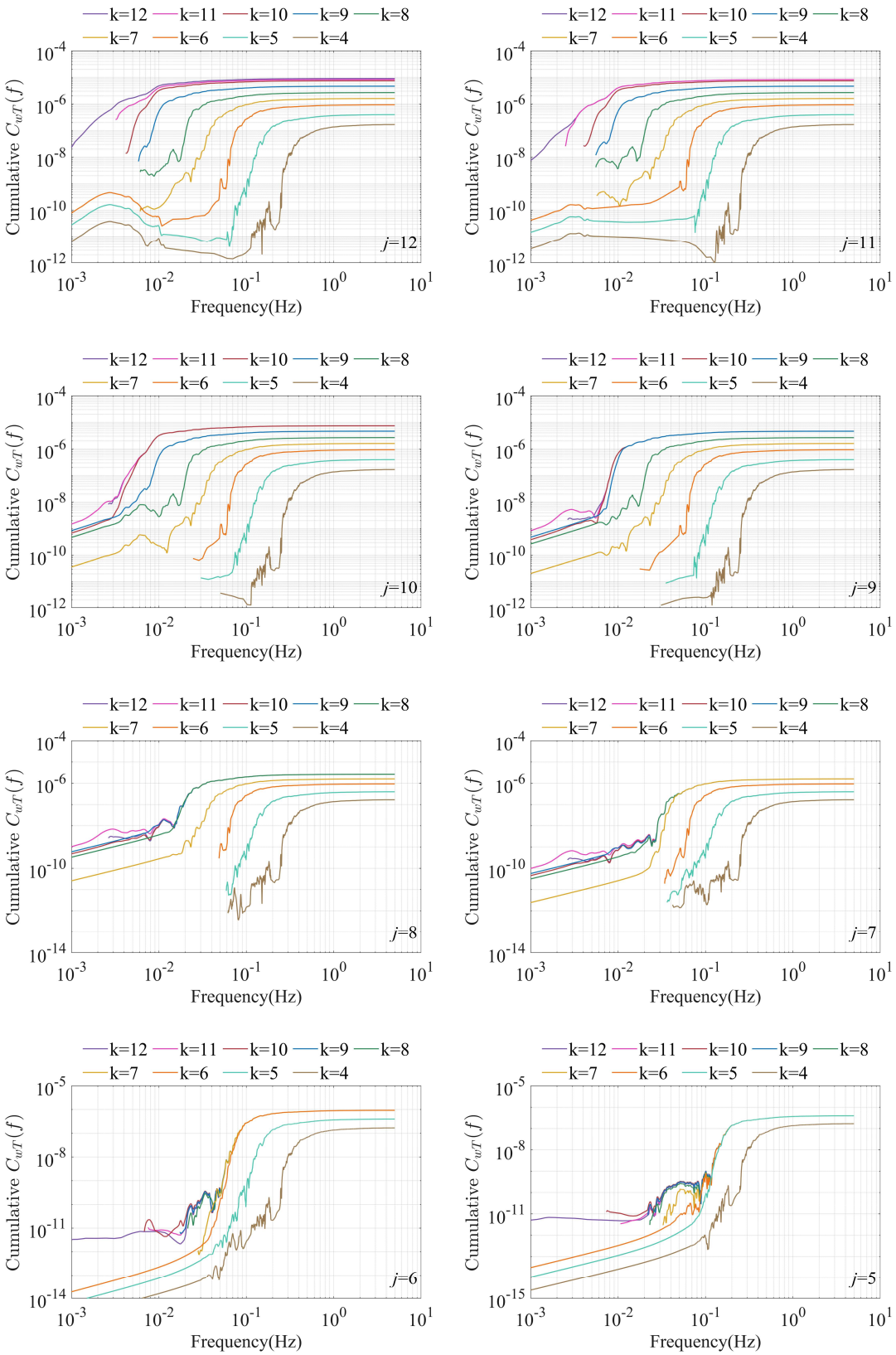
k=12 k=11 k=10 k=9 k=8
k=7 k=6 k=5 k=4
Cumulative $C_{wT}(f)$
Frequency(Hz)
j=12
j=11
j=10
j=9
j=8
j=7
j=6
j=5

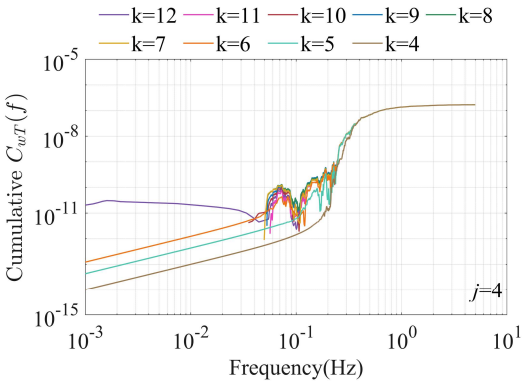

(b) Event 2: June 7, 2017, 16:00 to 18:00, Pattern 2 wind profile (Unstable)

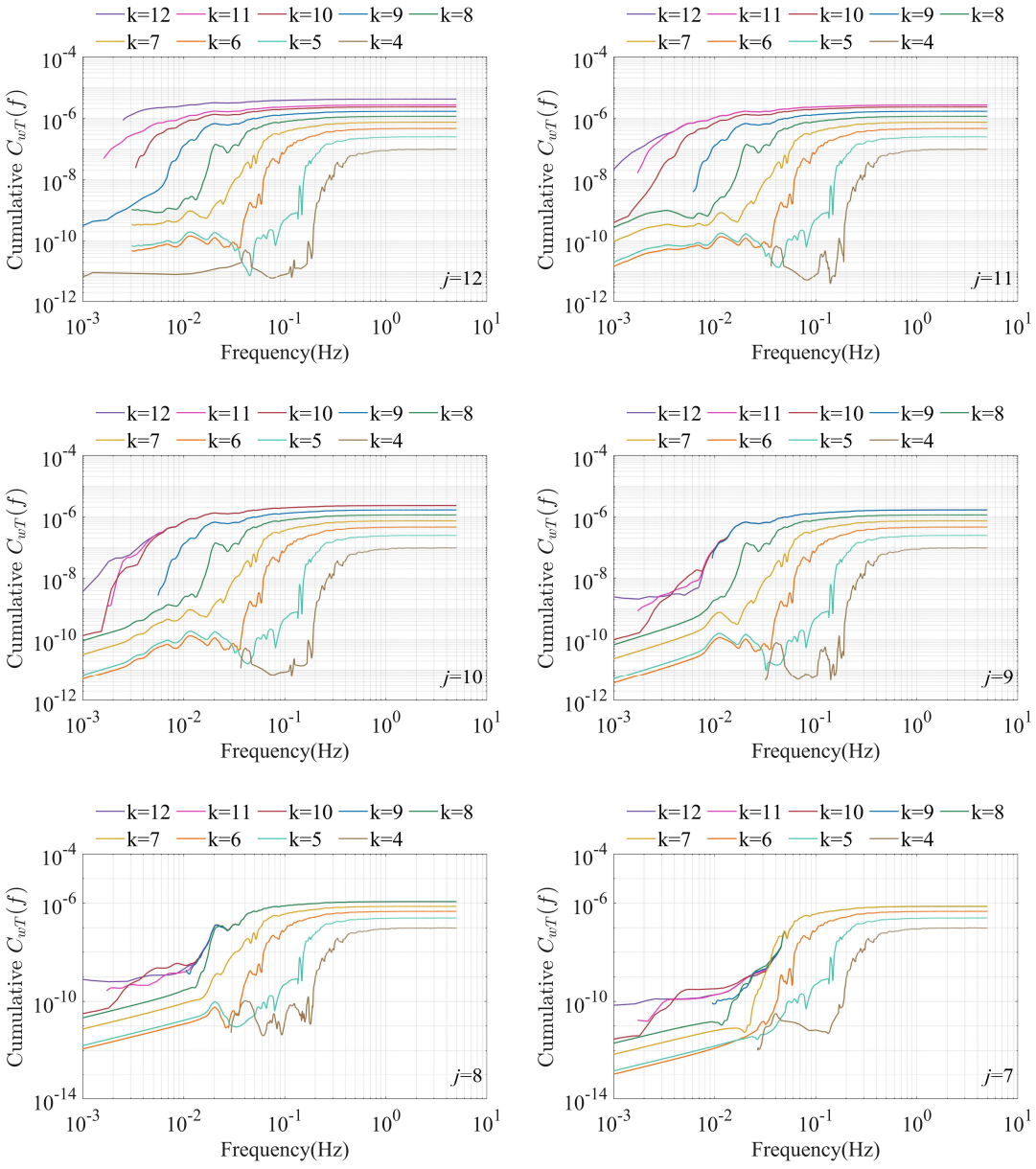

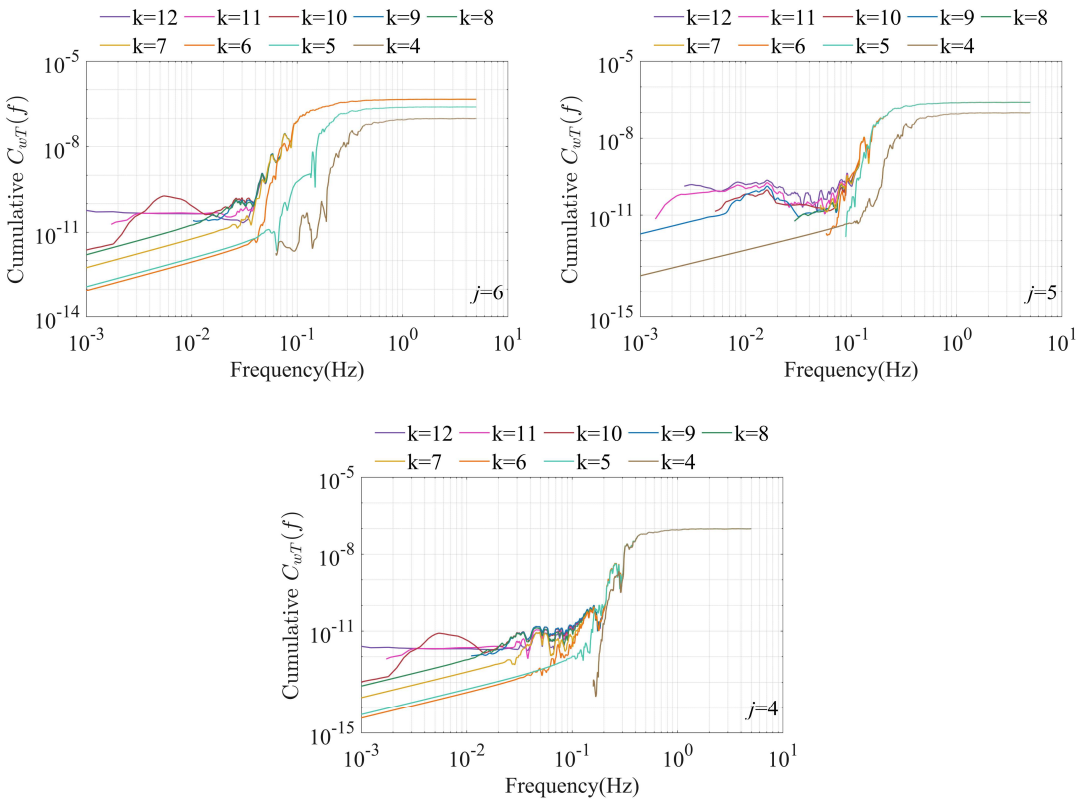

(c) Event 3: May 20, 2017, 1:00 to 3:00, Jet-type wind profile (Stable)

Fig. A2 Cumulative cospectrum of three typical time series

A3.Derivation of the Universal Function for Unstable Stratification

The Richardson number (R_i) is likewise a stability index based on the relative behavior of momentum and heat. Its computation is given in Eq.(46). Under the similarity hypothesis (Eq.(27)), the vertical gradients of temperature and wind speed can be expressed in terms of the universal functions for momentum (Φ_m) and heat (Φ_h), which ultimately allows R_i to be rewritten in a form involving the Obukhov length (Eq.(4)) together with the universal functions. The detailed derivation is presented in connection with Eq.(46).

$$
\begin{aligned}
R_i &= \frac{g}{\overline{T}}\frac{\partial T}{\partial z}\Big/\left(\frac{\partial u}{\partial z}\right)^2 \\
&= \frac{g}{\overline{T}}\frac{\Phi_h T_*}{\kappa z}\Big/\left(\frac{\Phi_m u_*}{\kappa z}\right)^2 \quad (T_* = \overline{w'T'}) \\
&= \frac{\Phi_h}{\Phi_m{}^2}\frac{\kappa T_* g/\overline{T}}{u_*^2} z \\
&= \frac{\Phi_h}{\Phi_m{}^2}\frac{z}{L}
\end{aligned}
\tag{46}
$$

825 Under similarity theory, the ratio of turbulent exchange coefficients is identical to the ratio of
826 universal functions, allowing the relationship between the Richardson number and the universal
827 function to be derived, as shown in Eq.(47).

$$\begin{aligned} &\frac{\Phi_h}{\Phi_m} = \frac{K_h}{K_m} = \gamma \\ &\mathrm{Ri} = \frac{\gamma\zeta}{\Phi_m} \quad (\zeta = \frac{z}{L}) \end{aligned} \tag{47}$$

828 Based on the Businger-Dyer relationship [93], the Richardson number under different
829 atmospheric stability conditions is expressed as a function of ζ as follows.

$$\begin{cases} \frac{z}{L} = \frac{R_i}{1 - c \cdot Ri} \quad (Ri \geq 0, Stable) \\ \frac{z}{L} = R_i \quad (Ri < 0, Unstable) \end{cases} \tag{48}$$

830 Substituting Eq.(47) into the turbulent equilibrium equation for the boundary layer atmosphere
831 [77], the equation can be rewritten in the form of Eq.(49).

$$\begin{aligned} &\Phi_m^4 - \delta\zeta\Phi_m^3 = 1 \\ &\rightarrow \Phi_m^4 - \frac{\delta}{\gamma} Ri \Phi_m^4 = 1 \end{aligned} \tag{49}$$

832 Substituting Eq.(48) into Eq.(49) yields a specific solution for the universal function under
833 unstable conditions in terms of the Richardson number, as shown in Eq.(46). Moreover, if a linear
834 transformation is introduced, like $a\Phi_m$, it does not affect the similarity criterion in Eq.(28) or the
835 validity of Eq.(49).

$$\begin{aligned} &\Phi_m = \left(1 - \frac{\delta}{\gamma}\mathrm{Ri}\right)^{-\frac{1}{4}} = \left(1 - \frac{\delta}{\gamma}\frac{z}{L}\right)^{-\frac{1}{4}} = (1 - b\frac{z}{L})^{-\frac{1}{4}} \\ &\rightarrow \Phi_m = a(1 - b\frac{z}{L})^{-\frac{1}{4}} (b > 0) \end{aligned} \tag{50}$$

836 **A4.Wind-profile correction accuracy**

837 Table A1-1 Wind-profile correction accuracy under the nonstationary method (50-230 m)

P1 (all)				P2 (all)			
Accuracy	Improved	B-D	Holtslag	Accuracy	Improved	B-D	Holtslag
R2	0.8845	0.3612	-0.2819	R2	0.9819	-0.5186	-0.7912
RMSE	0.3172	0.7908	1.0711	RMSE	0.1584	1.4523	1.5773

838 Table A1-2 Pattern 1 correction accuracy under the nonstationary method (50-230 m)

P1-Unstable				P1-Stable			
Accuracy	Improved	B-D	Holtslag	Accuracy	Improved	B-D	Holtslag
R2	0.9488	-1.6882	-1.8137	R2	0.8062	0.7175	-0.0111

RMSE	0.1766	1.2822	1.3093	RMSE	0.4122	0.4977	0.9415

839 Table A1-3 Pattern 2 correction accuracy under the nonstationary method (50-230 m)

P2-Unstable				P2-Stable			
Accuracy	Improved	B-D	Holtslag	Accuracy	Improved	B-D	Holtslag
R2	0.9400	-1.3390	-1.4695	R2	0.9579	0.7443	0.3388
RMSE	0.2736	1.7081	1.7553	RMSE	0.2323	0.5726	0.9207

840 Table A2-1 Wind-profile correction accuracy under the stationary method (50-230 m)

P1 (all)				P2 (all)			
Accuracy	Improved	B-D	Holtslag	Accuracy	Improved	B-D	Holtslag
R2	0.8852	0.4489	0.0809	R2	0.9465	0.1378	-0.1269
RMSE	0.3253	0.7127	0.9204	RMSE	0.2721	1.0922	1.2492

841 Table A2-2 Pattern 1 correction accuracy under the stationary method (50-230 m)

P1-Unstable				P1-Stable			
Accuracy	Improved	B-D	Holtslag	Accuracy	Improved	B-D	Holtslag
R2	0.9828	-1.2915	-1.4381	R2	0.8495	0.7675	0.7893
RMSE	0.1052	1.2133	1.2513	RMSE	0.3613	0.4487	0.4271

842 Table A2-3 Pattern 2 correction accuracy under the stationary method (50-230 m)

P2-Unstable				P2-Stable			
Accuracy	Improved	B-D	Holtslag	Accuracy	Improved	B-D	Holtslag
R2	0.9503	-0.8029	-0.9542	R2	0.9743	0.9730	0.8650
RMSE	0.2512	1.5131	1.5755	RMSE	0.1794	0.1842	0.4114

843

844

References:

[1] G. Poulos, S. S. Zhong, An observational history of small-scale katabatic winds in mid-latitudes, Geography Compass, 2 (2008) 1798-1821. https://doi.org/10.1111/j.1749-8198.2008.00166.x

[2] B. Yan, J. Su, H. Zhu, et al., Numerical study of wake characteristics of wind turbines in a real complex terrain with large eddy simulation, Physics of Fluids, 37 (2025).

[3] T. Yan, J. Qin, M. Zhang, et al., Field measurement analysis of wind profiles in mountainous terrain: focusing on periodic thermally-developed winds, Journal of Wind Engineering and Industrial Aerodynamics, 262 (2025) 106108. https://doi.org/10.1016/j.jweia.2025.106108

[4] L. Mahrt, Stratified atmospheric boundary layers and breakdown of models, Theoretical and Computational Fluid Dynamics, 11 (1998) 263-279. 10.1007/s001620050093

[5] A. A. Shestakova, P. A. Toropov, V. M. Stepanenko, et al., Observations and modelling of downslope windstorm in novorossiysk, Dynamics of Atmospheres and Oceans, 83 (2018) 83-99. https://doi.org/10.1016/j.dynatmoce.2018.07.001

[6] M. Zhang, J. Zhang, Y. Li, et al., Multi-site measurement for energy application of small distributed wind farm in complex mountainous areas, Energy Reports, 6 (2020) 1043-1056. https://doi.org/10.1016/j.egyr.2020.04.019

[7] D. Finn, K. L. Clawson, R. G. Carter, et al., Plume dispersion anomalies in a nocturnal urban boundary layer in complex terrain, Journal of Applied Meteorology and Climatology, 47 (2008) 2857-2878. https://doi.org/10.1175/2008JAMC1864.1

[8] Z. Lu, S. Li, J. Fu, et al., Wind-induced vibration control of bridge girders by aerodynamic and mechanical methods: a literature review, Advances in Bridge Engineering, 6 (2025) 35. 10.1186/s43251-025-00182-4

[9] M. S. Ahsanullah, N. B. Kaye, Measurements of shear stress distribution over a flat roof as a function of parapet height, wind direction, and roof roughness, Advances in Wind Engineering, 2 (2025) 100071. https://doi.org/10.1016/j.awe.2025.100071

[10] M. Liu, Y. Pan, J. Hu, et al., Field measurement study of intense thunderstorm outflows characteristics based on 356 m high meteorological tower, Journal of Wind Engineering and Industrial Aerodynamics, 242 (2023) 105590. 10.1016/j.jweia.2023.105590

[11] M. Zhang, J. Zhang, F. Jiang, et al., Combined wind profile characteristics based on wind parameters joint probability model in a mountainous gorge, Natural Hazards (Dordrecht), 115 (2023) 709-733. 10.1007/s11069-022-05571-w

[12] J. Zhang, M. Zhang, Y. Li, et al., Analysis of wind characteristics and wind energy potential in complex mountainous region in southwest china, Journal of Cleaner Production, 274 (2020) 123036. 10.1016/j.jclepro.2020.123036

[13] K. Wang, K. Yang, Q. Wang, et al., Turbulence characteristics of nonstationary wind at gobi desert wind power cluster: a doppler wind lidar measurement, Physics of Fluids, 37 (2025).

[14] B. Zhang, L. Wang, J. Ge, et al., Advanced wake modeling in wind farm: a physics-informed framework with virtual lidar measurements, Physics of Fluids, 37 (2025).

[15] A. S. Monin, A. M. Obukhov, Basic laws of turbulent mixing in the surface layer of the atmosphere, Contrib. Geophys. Inst. Acad. Sci. Ussr, 151 (1954) e187.

[16] R. B. Stull, An introduction to boundary layer meteorology, Springer Science & Business Media(2012).

[17] R. B. Stull, Similarity theory, An Introduction to Boundary Layer Meteorology, Springer Netherlands, Dordrecht(1988). pp. 347-404. 10.1007/978-94-009-3027-8_9
[18] M. B. Parlange, G. G. Katul, Watershed scale shear stress from tethersonde wind profile measurements under near neutral and unstable atmospheric stability, Water Resources Research, 31 (1995) 961-968. 10.1029/94WR01949
[19] R. B. Stull, Boundary conditions and surface forcings, An Introduction to Boundary Layer Meteorology, Springer Netherlands, Dordrecht(1988). pp. 251-294. 10.1007/978-94-009-3027-8_7
[20] Z. R. Shu, Q. S. Li, Y. C. He, et al., Investigation of low-level jet characteristics based on wind profiler observations, Journal of Wind Engineering and Industrial Aerodynamics, 174 (2018) 369-381. https://doi.org/10.1016/j.jweia.2018.01.035
[21] J. A. Businger, J. C. Wyngaard, Y. Izumi, et al., Flux-profile relationships in the atmospheric surface layer, Journal of Atmospheric Sciences, 28 (1971) 181-189.
[22] M. P. Araújo Da Silva, A. Salcedo-Bosch, F. Rocadenbosch, et al., On the retrieval of surface-layer parameters from lidar wind-profile measurements, Remote Sensing, 15 (2023) 2660.
[23] M. C. Holtslag, W. A. A. M. Bierbooms, G. J. W. van Bussel, Validation of surface layer similarity theory to describe far offshore marine conditions in the dutch north sea in scope of wind energy research, Journal of Wind Engineering and Industrial Aerodynamics, 136 (2015) 180-191. https://doi.org/10.1016/j.jweia.2014.10.013
[24] S. T. Salesky, M. Chamecki, Random errors in turbulence measurements in the atmospheric surface layer: implications for monin-obukhov similarity theory, Journal of the Atmospheric Sciences, 69 (2012) 3700-3714. 10.1175/JAS-D-12-096.1
[25] D. G. Steyn, S. F. J. De Wekker, M. Kossmann, et al., Boundary layers and air quality in mountainous terrain, Mountain Weather Research and Forecasting: Recent Progress and Current Challenges, Springer Netherlands, Dordrecht(2013). pp. 261-289. 10.1007/978-94-007-4098-3_5
[26] A. M. Yaglom, Comments on wind and temperature flux-profile relationships, Boundary-Layer Meteorology, 11 (1977) 89-102.
[27] S. Rafailidis, Influence of building areal density and roof shape on the wind characteristics above a town, Boundary-Layer Meteorology, 85 (1997) 255-271. 10.1023/A:1000426316328
[28] L. Soulhac, R. J. Perkins, P. Salizzoni, Flow in a street canyon for any external wind direction, Boundary-Layer Meteorology, 126 (2008) 365-388. 10.1007/s10546-007-9238-x
[29] Q. Ke, X. Shi, J. Lei, et al., Influence of atmospheric stratification and air-sea interaction on sea surface wind profile, Journal of Tropical Meteorology, 36 (2020) 370-376. 10.16032/j.issn.1004-4965.2020.035
[30] C. A. Lopez-Villalobos, O. Martínez-Alvarado, O. Rodriguez-Hernandez, et al., Analysis of the influence of the wind speed profile on wind power production, Energy Reports, 8 (2022) 8079-8092. 10.1016/j.egyr.2022.06.046
[31] Z. Gao, X. Qian, T. Wang, Spectral partition characteristics of wind turbine load response under different atmospheric stability, Sustainable Energy Technologies and Assessments, 47 (2021) 101421. https://doi.org/10.1016/j.seta.2021.101421
[32] Y. Zheng, W. Li, C. Fang, et al., Investigating the impact of weather conditions on urban heat island development in the subtropical city of hong kong, Atmosphere, 14 (2023) 257.
[33] T. Kiyota, N. Kiyota, A study on influence of land and sea breeze on air temperature in hiroshima wide area in summer season, Journal of Environmental Engineering (Transactions of Aij), 70 (2005) 45-51. 10.3130/aije.70.45_1

[34] Y. Li, F. Jiang, M. Zhang, et al., Observations of periodic thermally-developed winds beside a bridge region in mountain terrain based on field measurement, Journal of Wind Engineering and Industrial Aerodynamics, 225 (2022) 104996. https://doi.org/10.1016/j.jweia.2022.104996
[35] D. Zardi, C. D. Whiteman, Diurnal mountain wind systems, Mountain Weather Research and Forecasting: Recent Progress and Current Challenges, Springer Netherlands, Dordrecht(2013). pp. 35-119. 10.1007/978-94-007-4098-3_2
[36] G. Huang, Y. Jiang, L. Peng, et al., Characteristics of intense winds in mountain area based on field measurement: focusing on thunderstorm winds, Journal of Wind Engineering and Industrial Aerodynamics, 190 (2019) 166-182. 10.1016/j.jweia.2019.04.020
[37] J. He, H. Zhang, D. Zhou, et al., Remote sensing information-aided numerical simulation of road wind environment in a complex forest area, Physics of Fluids, 37 (2025).
[38] F. Jiang, J. Zhang, M. Zhang, et al., Determination of extreme wind speed under different wind directions and attack angles with mixed wind climates in mountain terrain, Stochastic Environmental Research and Risk Assessment, 37 (2023) 4589-4606. 10.1007/s00477-023-02529-7
[39] J. Weinkaemmerer, I. B. Ďurán, J. Schmidli, The impact of large-scale winds on boundary layer structure, thermally driven flows, and exchange processes over mountainous terrain, Journal of the Atmospheric Sciences, 79 (2022) 2685-2701. https://doi.org/10.1175/JAS-D-21-0195.1
[40] M. P. Meyers, W. J. Steenburgh, Mountain weather prediction: phenomenological challenges and forecast methodology, Mountain Weather Research and Forecasting: Recent Progress and Current Challenges, Springer Netherlands, Dordrecht(2013). pp. 1-34. 10.1007/978-94-007-4098-3_1
[41] P. Bougeault, A. Jansa, J. Attié, et al., The atmospheric momentum budget over a major mountain range: first results of the pyrex field program, Annales geophysicae(1993), pp. 395-418.
[42] J. Zhang, F. Jiang, M. Zhang, et al., Study on joint design method of multiple wind parameters for long-span bridges in deep-cutting gorge areas based on field measurement, Journal of Wind Engineering and Industrial Aerodynamics, 254 (2024) 105930. https://doi.org/10.1016/j.jweia.2024.105930
[43] J. S. Bendat, A. G. Piersol, Random data: analysis and measurement procedures, John Wiley & Sons(2011).
[44] Y. Song, Z. Ti, H. Deng, et al., Vortex-induced vibrations of sea-crossing bridge deck subject to dynamic wave boundary layer airflows, Physics of Fluids, 37 (2025).
[45] J. Pan, Z. Ti, K. Wei, et al., Dynamic response modeling of sea-crossing bridge pier under the combined action of earthquakes and ocean waves using high-order time-domain boundary element method, Marine Structures, 103 (2025) 103823.
[46] J. D. Holmes, Wind loading of structures, CRC press(2007).
[47] R. B. Stull, Mean boundary layer characteristics, An Introduction to Boundary Layer Meteorology, Springer Netherlands, Dordrecht(1988). pp. 1-27. 10.1007/978-94-009-3027-8_1
[48] F. Jiang, M. Zhang, Y. Li, et al., Field measurement analysis of wind parameters and nonstationary characteristics in mountainous terrain: focusing on cooling windstorms, Journal of Wind Engineering and Industrial Aerodynamics, 230 (2022). 10.1016/j.jweia.2022.105175
[49] Y. Su, G. Huang, Y. Xu, Derivation of time-varying mean for nonstationary downburst winds, Journal of Wind Engineering and Industrial Aerodynamics, 141 (2015) 39-48. https://doi.org/10.1016/j.jweia.2015.02.008
[50] L. Chen, C. W. Letchford, Proper orthogonal decomposition of two vertical profiles of full-scale nonstationary downburst wind speeds[lzcl], Journal of Wind Engineering and Industrial Aerodynamics, 93 (2005) 187-216. https://doi.org/10.1016/j.jweia.2004.11.004

[51] Z. Wu, N. E. Huang, Ensemble empirical mode decomposition: a noise-assisted data analysis method, Advances in Adaptive Data Analysis, 1 (2009) 1-41. 10.1142/S1793536909000047
[52] S. Hanifi, H. Zare-Behtash, A. Cammarano, et al., Offshore wind power forecasting based on wpd and optimised deep learning methods, Renewable Energy, 218 (2023) 119241.
[53] S. Cheng, V. S. Neary, L. P. Chamorro, On detrending stream velocity time series for robust tidal flow turbulence characterization, Ocean Engineering, 300 (2024) 117427.
[54] Z. Liu, H. Zhang, X. Cai, et al., Quantitative evaluation of turbulence reconstruction algorithms for flux estimation based on the characteristics of atmospheric turbulence, Physics of Fluids, 37 (2025).
[55] S. Cheng, Y. S. Jetti, V. S. Neary, et al., Incorporating long-range dependence and fractal features in turbulence spectra, Scientific Reports, 15 (2025) 31663.
[56] W. Zhang, Z. Qu, K. Zhang, et al., A combined model based on ceemdan and modified flower pollination algorithm for wind speed forecasting, Energy Conversion and Management, 136 (2017) 439-451.
[57] F. Jiang, J. Zhang, M. Zhang, et al., Field measurement study on classification for mixed intense wind climate in mountainous terrain, Measurement, 217 (2023) 113064. 10.1016/j.measurement.2023.113064
[58] F. Jiang, M. Zhang, Y. Li, et al., Field measurement study of wind characteristics in mountain terrain: focusing on sudden intense winds, Journal of Wind Engineering and Industrial Aerodynamics, 218 (2021). 10.1016/j.jweia.2021.104781
[59] A. Fenerci, O. Øiseth, A. Rønnquist, Long-term monitoring of wind field characteristics and dynamic response of a long-span suspension bridge in complex terrain, Engineering Structures, 147 (2017) 269-284. 10.1016/j.engstruct.2017.05.070
[60] F. Jiang, J. Zhang, M. Zhang, et al., Field measurement study on classification for mixed intense wind climate in mountainous terrain, Measurement, 217 (2023) 113064. 10.1016/j.measurement.2023.113064
[61] A. Fenerci, O. Øiseth, Site-specific data-driven probabilistic wind field modeling for the wind-induced response prediction of cable-supported bridges, Journal of Wind Engineering and Industrial Aerodynamics, 181 (2018) 161-179. 10.1016/j.jweia.2018.09.002
[62] M. Zhang, J. Zhang, H. Chen, et al., Probabilistic wind spectrum model based on correlation of wind parameters in mountainous areas: focusing on von karman spectrum, Journal of Wind Engineering and Industrial Aerodynamics, 234 (2023) 105337. https://doi.org/10.1016/j.jweia.2023.105337
[63] J. V. Bradley, Distribution-free statistical tests, United States Air Force(1960).
[64] F. K. Chow, S. F. J. De Wekker, B. J. Snyder, Mountain weather research and forecasting, 1 ed., Springer Dordrecht(2013). https://doi.org/10.1007/978-94-007-4098-3
[65] A. Boggess, F. J. Narcowich, A first course in wavelets with fourier analysis, Wiley(2011).
[66] F. Jiang, M. Zhang, Y. Li, et al., Field measurement analysis of wind parameters and nonstationary characteristics in mountainous terrain: focusing on cooling windstorms, Journal of Wind Engineering and Industrial Aerodynamics, 230 (2022) 105175. https://doi.org/10.1016/j.jweia.2022.105175
[67] S. Brusco, G. Buresti, G. Piccardo, Thunderstorm-induced mean wind velocities and accelerations through the continuous wavelet transform, Journal of Wind Engineering and Industrial Aerodynamics, 221 (2022) 104886. https://doi.org/10.1016/j.jweia.2021.104886
[68] G. Huang, H. Zheng, Y. L. Xu, et al., Spectrum models for nonstationary extreme winds, Journal of Structural Engineering (United States), 141 (2015). 10.1061/(ASCE)ST.1943-541X.0001257
[69] M. B. Priestley, Evolutionary spectra and nonstationary processes, Journal of the Royal Statistical

Society: Series B (Methodological), 27 (1965) 204-229.
[70] M. B. Priestley, Design relations for nonstationary processes, Journal of the Royal Statistical Society Series B: Statistical Methodology, 28 (1966) 228-240.
[71] G. Huang, X. Chen, Wavelets-based estimation of multivariate evolutionary spectra and its application to nonstationary downburst winds, Engineering Structures, 31 (2009) 976-989. https://doi.org/10.1016/j.engstruct.2008.12.010
[72] Y. Su, G. Huang, Y. L. Xu, Derivation of time-varying mean for nonstationary downburst winds, Journal of Wind Engineering and Industrial Aerodynamics, 141 (2015) 39-48. 10.1016/j.jweia.2015.02.008
[73] R. B. Stull, Turbulence kinetic energy, stability and scaling, An Introduction to Boundary Layer Meteorology, Springer Netherlands, Dordrecht(1988). pp. 151-195. 10.1007/978-94-009-3027-8_5
[74] T. W. HORST, A simple formula for attenuation of eddy fluxes measured with first-order-response scalar sensors, Boundary-Layer Meteorology, 82 (1997) 219-233. 10.1023/A:1000229130034
[75] R. B. Stull, Some mathematical & conceptual tools: part 2. Time series, An Introduction to Boundary Layer Meteorology, Springer Netherlands, Dordrecht(1988). pp. 295-345. 10.1007/978-94-009-3027-8_8
[76] A. M. Obukhov, Turbulence in an atmosphere with a non-uniform temperature, Boundary-Layer Meteorology, 2 (1971) 7-29. 10.1007/BF00718085
[77] H. A. Panofsky, J. A. Dutton, Atmospheric turbulence john wiley, New York, (1984).
[78] Z. Wei, H. Zhang, Y. Ren, et al., Study on the characteristics of the pressure fluctuations and their contribution to turbulence kinetic energy, Atmospheric Research, 258 (2021) 105634. https://doi.org/10.1016/j.atmosres.2021.105634
[79] O. C. Acevedo, F. D. Costa, P. E. S. Oliveira, et al., The influence of submeso processes on stable boundary layer similarity relationships, Journal of the Atmospheric Sciences, 71 (2014) 207-225. https://doi.org/10.1175/JAS-D-13-0131.1
[80] Z. Wei, L. Zhang, Y. Ren, et al., Characteristics of the turbulence intermittency and its influence on the turbulent transport in the semi-arid region of the loess plateau, Atmospheric Research, 249 (2021) 105312. https://doi.org/10.1016/j.atmosres.2020.105312
[81] J. A. Businger, J. C. Wyngaard, Y. Izumi, et al., Flux-profile relationships in the atmospheric surface layer, Journal of Atmospheric Sciences, 28 (1971) 181-189.
[82] A. J. Dyer, A review of flux-profile relationships, Boundary-Layer Meteorology, 7 (1974) 363-372. 10.1007/BF00240838
[83] L. Mahrt, Stratified atmospheric boundary layers and breakdown of models, Theoretical and Computational Fluid Dynamics, 11 (1998) 263-279. 10.1007/s001620050093
[84] T. Yan, J. Qin, M. Zhang, et al., Investigation of wind profile and turbulent transport patterns in complex mountainous terrain based on clustering analysis, Journal of Wind Engineering and Industrial Aerodynamics, 268 (2026) 106289. https://doi.org/10.1016/j.jweia.2025.106289
[85] L. Mahrt, Stratified atmospheric boundary layers and breakdown of models, Theoretical and Computational Fluid Dynamics, 11 (1998) 263-279. 10.1007/s001620050093
[86] R. Snaiki, T. Wu, A semi-empirical model for mean wind velocity profile of landfalling hurricane boundary layers, Journal of Wind Engineering and Industrial Aerodynamics, 180 (2018) 249-261. https://doi.org/10.1016/j.jweia.2018.08.004
[87] P. J. Vickery, D. Wadhera, M. D. Powell, et al., A hurricane boundary layer and wind field model for use in engineering applications, Journal of Applied Meteorology and Climatology, 48 (2009) 381-

405. https://doi.org/10.1175/2008JAMC1841.1
[88] S. Gryning, E. Batchvarova, B. Brümmer, et al., On the extension of the wind profile over homogeneous terrain beyond the surface boundary layer, Boundary-Layer Meteorology, 124 (2007) 251-268. 10.1007/s10546-007-9166-9
[89] N. Cliff, Dominance statistics: ordinal analyses to answer ordinal questions., Psychological Bulletin, 114 (1993) 494.
[90] J. Cohen, Statistical power analysis for the behavioral sciences, routledge(2013).
[91] M. Tomczak, E. Tomczak, The need to report effect size estimates revisited. An overview of some recommended measures of effect size, (2014).
[92] J. C. Wyngaard, On the surface-layer turbulence, Workshop on micrometeorology, Amer. Meteorol. Soc.(1973), pp. 101-149.
[93] S. P. Arya, Atmospheric boundary layers over homogeneous terrain, (1982).
[94] A. A. M. Holtslag, Estimates of diabatic wind speed profiles from near-surface weather observations, Boundary-Layer Meteorology, 29 (1984) 225-250. 10.1007/BF00119790
[95] A. Holtslag, H. De Bruin, Applied modeling of the nighttime surface energy balance over land, Journal of Applied Meteorology and Climatology, 27 (1988) 689-704.